

# A giant planet transiting a 3 Myr protostar with a misaligned disk

Madyson G. Barber<sup>1,2</sup>, Andrew W. Mann<sup>1</sup>, Andrew Vanderburg<sup>3</sup>, Daniel Krolikowski<sup>4</sup>, Adam Kraus<sup>5</sup>, Megan Ansdell<sup>6</sup>, Logan Pearce<sup>4</sup>, Gregory N. Mace<sup>5</sup>, Sean M. Andrews<sup>7</sup>, Andrew W. Boyle<sup>1</sup>, Karen A. Collins<sup>7</sup>, Matthew De Furio<sup>5</sup>, Diana Dragomir<sup>8</sup>, Catherine Espaillat<sup>9</sup>, Adina D. Feinstein<sup>10,11</sup>, Matthew Fields<sup>1</sup>, Daniel Jaffe<sup>5</sup>, Ana Isabel Lopez Murillo<sup>1</sup>, Felipe Murgas<sup>12,13</sup>, Elisabeth R. Newton<sup>14</sup>, Enric Palle<sup>12,13</sup>, Erica Sawczynec<sup>5</sup>, Richard P. Schwarz<sup>7</sup>, Pa Chia Thao<sup>1,2</sup>, Benjamin M. Tofflemire<sup>5,15</sup>, Cristilyn N. Watkins<sup>7</sup>, Jon M. Jenkins<sup>16</sup>, David W. Latham<sup>7</sup>, George Ricker<sup>3</sup>, Sara Seager<sup>3,18,19</sup>, Roland Vanderspek<sup>3</sup>, Joshua N. Winn<sup>20</sup>, David Charbonneau<sup>7</sup>, Zahra Essack<sup>8</sup>, David R. Rodriguez<sup>17</sup>, Avi Shporer<sup>3</sup>, Joseph D. Twicken<sup>16,21</sup>, Jesus Noel Vilaseñor<sup>3</sup>

<sup>1</sup>Department of Physics and Astronomy, University of North Carolina at Chapel Hill, Chapel Hill, NC 27599, USA

<sup>2</sup>NSF Fellow

<sup>3</sup>Department of Physics and Kavli Institute for Astrophysics and Space Research, Massachusetts Institute of Technology, Cambridge, MA 02139, USA

<sup>4</sup>Steward Observatory, The University of Arizona, 933 N. Cherry Ave, Tucson, AZ 85721, USA

<sup>5</sup>Department of Astronomy, The University of Texas at Austin, Austin, TX 78712, USA

<sup>6</sup>NASA Headquarters, 300 E Street SW, Washington, DC 20546, USA

<sup>7</sup>Center for Astrophysics | Harvard & Smithsonian, 60 Garden Street, Cambridge, MA 02138, USA

<sup>8</sup>Department of Physics and Astronomy, The University of New Mexico, 210 Yale Blvd NE, Albuquerque, NM 87106, USA

<sup>9</sup>Institute for Astrophysical Research, Department of Astronomy, Boston University, 725 Commonwealth Avenue, Boston, MA 02215, USA

<sup>10</sup>Laboratory for Atmospheric and Space Physics, University of Colorado Boulder, UCB 600, Boulder, CO 80309

<sup>11</sup>NHFP Sagan Fellow

<sup>12</sup>Instituto de Astrofísica de Canarias (IAC), E-38205 La Laguna, Tenerife, Spain

<sup>13</sup>Departamento de Astrofísica, Universidad de La Laguna (ULL), E-38206 La Laguna, Tenerife, Spain

<sup>14</sup>Department of Physics and Astronomy, Dartmouth College, Hanover, NH 03755, USA

<sup>15</sup>51 Pegasi b Fellow

<sup>16</sup>NASA Ames Research Center, Moffett Field, CA, 94035, USA

<sup>17</sup>Space Telescope Science Institute, 3700 San Martin Drive, Baltimore, MD, 21218, USA

<sup>18</sup>Department of Earth, Atmospheric and Planetary Sciences, Massachusetts Institute of Technology, Cambridge, MA 02139, USA

<sup>19</sup>Department of Aeronautics and Astronautics, Massachusetts Institute of Technology, Cambridge, MA 02139, USA

<sup>20</sup>Department of Astrophysical Sciences, Princeton University, 4 Ivy Lane, Princeton, NJ 08544, USA

<sup>21</sup>SETI Institute, Mountain View, CA 94043 USA

Astronomers have found more than a dozen planets transiting 10-40 million year old stars <sup>1</sup>, but younger transiting planets have remained elusive. The lack of such discoveries may be because planets have not fully formed at this age or that our view is blocked by the protoplanetary disk. However, we now know that many outer disks are warped/broken <sup>2</sup>; provided the inner disk is depleted, transiting planets may thus be visible. Here we report the observations of the transiting planet IRAS 04125+2902 b orbiting a 3 Myr,  $0.7 M_{\odot}$ , pre-main sequence star in the Taurus Molecular Cloud. The host star harbors a nearly face-on ( $i \simeq 30^\circ$ ) transitional disk <sup>3</sup> and a wide binary companion. The planet has a period of 8.83 days, a radius of  $10.7 R_{\oplus}$  ( $0.96 R_J$ ), and a 95%-confidence upper limit on its mass of  $90 M_{\oplus}$  ( $0.3 M_J$ ) from radial velocity measurements, making it a possible precursor of the super-Earths and sub-Neptunes commonly found around main-sequence stars. The rotational broadening of the star and the orbit of the wide ( $4''$ , 635 AU) companion are both consistent with edge-on orientations. Thus, all components of the system are consistent with alignment except the outer disk; the origin of this misalignment is unclear.

## 1 Main

IRAS 04125+2902 was first observed by NASA’s Transiting Exoplanet Survey Satellite (*TESS*) in November 2019, and since then, *TESS* has detected 17 transits of IRAS 04125+2902 b across six sectors (Figure 1). Follow-up observations using the Las Cumbres Observatory (LCO) 1-meter telescopes confirmed with higher angular resolution that the star is the source of the photometric variations seen by *TESS* and has a consistent depth at wavelengths  $0.5 - 0.9\mu\text{m}$  (Figure 2). Our analysis of the light curve indicates that the planet orbits its star every 8.83 days and has a radius of  $0.96 \pm 0.08 R_J$ . The multi-color observations of transits, radial velocities (RVs), and multi-epoch high-resolution imaging combine to rule out all known false positive scenarios (see Methods).

IRAS 04125+2902 is a T-Tauri star inside the Taurus-Auriga star-forming region. Taurus-Auriga itself is made up of at least 17 distinct subpopulations ranging in age from 1.3 to 15 Myr. The star is a member of the D4-North subpopulation, with an estimated age of  $2.49_{-0.34}^{+0.35}$  Myr<sup>4</sup>. By comparing the spectra, photometry, and *Gaia* parallax to a grid of evolutionary models<sup>5</sup>, we determined an age of  $3.3_{-0.5}^{+0.6}$  Myr for the host star, consistent with the group age at  $1.3\sigma$ .

This makes IRAS 04125+2902 b the youngest transiting planet discovered to date by a factor of  $\simeq 3$ . There are similar-age directly imaged systems<sup>6,7</sup>, but they reside near the boundary between brown dwarfs and planets. Radial velocity surveys have also uncovered similar-aged non-transiting planet candidates<sup>8,9</sup>, but those remain controversial<sup>10,11</sup>. Even if confirmed, those planets are  $> 1M_J$ , making them progenitors of brown dwarfs or hot Jupiters.

The analysis of archival and new RVs sets an upper limit of  $< 0.3 M_J$  on the planet’s mass. Planets younger than  $\sim 100$  Myr are expected to have inflated radii and will shrink over time<sup>12</sup>. Gas-giant planet progenitors ( $\gtrsim 1M_J$ ) are expected to be  $1.4-2R_J$  for their first 20-30 Myr<sup>13</sup>. Observational data shows 10-700 Myr planets are larger and have a lower density than their older counterparts<sup>14</sup>. Further, small planets are intrinsically more common, particularly around lower-mass stars, so the likelihood of finding a hot Jupiter orbiting a  $0.7M_\odot$  star is small<sup>15</sup>. Thus the observational and statistical data indicate the planet is not a true giant, but instead a progenitor of a sub-Saturn ( $4 - 7R_\oplus$ ) or even a sub-Neptune ( $\simeq 1.5 - 4R_\oplus$ ).

Pebble accretion models can form and migrate a solid core of  $\sim$ tens of Earth masses to  $< 0.2\text{AU}$  within 2-3 Myr<sup>16</sup>. The existence of IRAS 04125+2902 b is not surprising in light of these models and provides observational evidence that planets can form and migrate on such a short timescale. It also demonstrates that a planet at this age can be a spherical object with a sharply defined photosphere (forming a trapezoid-like transit) rather than a cloud of dust and gas or a still-forming ring-like system<sup>17</sup>.

Protoplanetary disks dissipate from the inside out, creating large inner dust cavities, often tens of AU in diameter. Disks with such cavities are known as transition disks<sup>18</sup>. Stars with

transition disks have long been targeted by direct imaging planet searches, both because the cavity may have been cleared by a giant planet<sup>19</sup> and because the region is optically thin enough to detect such a planet<sup>20</sup>. The star shows clear evidence for a transition disk (Figure 3), based on its spectral energy distribution and on submillimeter observations of the outer disk <sup>3</sup>, but no directly-imaged planets inside the gap have been found to date <sup>21</sup>.

It was previously thought that the detection of a transiting planet in a disk-bearing system was improbable. A transiting planet must have a high orbital inclination (edge-on) and is assumed to have formed within the (sky-projected) plane of the disk, but an optically thick edge-on disk would also block observations of the host star at wavelengths of typical transit observations. However, the outer disk surrounding IRAS 04125+2902 is close to face-on when observed from Earth and has a depleted inner disk out to  $\simeq 20$  AU <sup>3</sup>.

The stellar rotational axis is consistent with that of the planet's orbital axis, but nearly perpendicular to the disk orientation (Figure 4, see Methods). The star has a 4'' binary companion, which could explain the disk misalignment. However, the orbit of the binary is also edge-on (see Methods), as has been seen in some other planetary systems with binary companions <sup>22</sup>. The lowest energy configuration is generally where system components are aligned <sup>23,24</sup>, suggesting the companion-disk interactions should preferentially push the disk *into* alignment with the binary's orbit.

The origin of the misaligned outer disk remains unclear. One possibility is that the inner and outer disk were initially aligned with each other and the orbital plane of the planet, but the planet became misaligned at a later phase (e.g., during migration). Current models for forming close-in sub-Neptunes tend to include migration of pebbles and/or planetesimals through the protoplanetary disk <sup>16</sup>, which produce planets aligned with their parent disk. Therefore, another massive object in the system likely would be required to move a planet into an orbit inclined from the disk that formed it, but there is no evidence of such an object in the system.

The alternative is that the outer disk became broken through a process distinct from interactions with the binary companion. Simulations of star-forming regions suggest outer disk warps could be common due to interactions between the early disk and the surrounding environment<sup>25</sup>, such as infalling material from the surrounding cloud <sup>26</sup>. Observational studies have also found increasing evidence of disk warps or breaks <sup>27,28</sup>, although others have found general alignment <sup>29</sup>. However, the frequency of outer disk misalignments at such young ages is not known. Thus, whether IRAS 04125+2902 is a special case or one of a larger population of systems with broken/warped disks <sup>30</sup> is still unclear.

Given its close proximity to Earth (160 pc) and rare configuration, the system is a powerful environment for understanding early formation and migration. Rossiter–McLaughlin measurements and future ALMA data can be used to further constrain the system alignment and disk

inclination. Due to the large radius and relatively low mass, we can conclude that the planet likely has a large extended atmosphere, ideal for follow-up with JWST. IRAS 04125+2902 b motivates further efforts to search the youngest stellar clusters for more of these infant planets.

1. Plavchan, P. *et al.* A planet within the debris disk around the pre-main-sequence star AU Microscopii. *Nature* **582**, 497–500 (2020).
2. Bohn, A. J. *et al.* Probing inner and outer disk misalignments in transition disks. Constraints from VLTI/GRAVITY and ALMA observations. *Astron. Astrophys.* **658**, A183 (2022).
3. Espaillat, C. *et al.* The Transitional Disk around IRAS 04125+2902. *Astrophys. J.* **807**, 156 (2015).
4. Krolkowski, D. M. *et al.* Gaia EDR3 Reveals the Substructure and Complicated Star Formation History of the Greater Taurus-Auriga Star-forming Complex. *Astron. J.* **162**, 110 (2021).
5. Bressan, A. *et al.* PARSEC: stellar tracks and isochrones with the PAdova and TRieste Stellar Evolution Code. *Mon. Not. R. Astron. Soc.* **427**, 127–145 (2012).
6. Kraus, A. L. *et al.* Three Wide Planetary-mass Companions to FW Tau, ROXs 12, and ROXs 42B. *Astrophys. J.* **781**, 20 (2014).
7. Fontanive, C. *et al.* A Wide Planetary-mass Companion to a Young Low-mass Brown Dwarf in Ophiuchus. *Astrophys. J.* **905**, L14 (2020).
8. Johns-Krull, C. M. *et al.* A Candidate Young Massive Planet in Orbit around the Classical T Tauri Star CI Tau. *Astrophys. J.* **826**, 206 (2016).
9. Donati, J. F. *et al.* A hot Jupiter orbiting a 2-million-year-old solar-mass T Tauri star. *Nature* **534**, 662–666 (2016).
10. Donati, J. F. *et al.* The magnetic field and accretion regime of CI Tau. *Mon. Not. R. Astron. Soc.* **491**, 5660–5670 (2020).
11. Damasso, M. *et al.* The GAPS Programme at TNG. XXVII. Reassessment of a young planetary system with HARPS-N: is the hot Jupiter V830 Tau b really there? *Astron. Astrophys.* **642**, A133 (2020).
12. Fortney, J. J. *et al.* Planetary Radii across Five Orders of Magnitude in Mass and Stellar Insolation: Application to Transits. *Astrophys. J.* **659**, 1661–1672 (2007).
13. Spiegel, D. S. & Burrows, A. Spectral and Photometric Diagnostics of Giant Planet Formation Scenarios.. *Astrophys. J.* **745**, 174 (2012).
14. Vach, S. *et al.* The Occurrence of Small, Short-period Planets Younger than 200 Myr with TESS. *Astron. J.* **167**, 210 (2024).

15. Fressin, F. *et al.* The False Positive Rate of Kepler and the Occurrence of Planets. *Astrophys. J.* **766**, 81 (2013).
16. Johansen, A. & Lambrechts, M. Forming Planets via Pebble Accretion.. *Annual Review of Earth and Planetary Sciences* **45**, 359–387 (2017).
17. Mamajek, E. E. *et al.* Planetary Construction Zones in Occultation: Discovery of an Extrasolar Ring System Transiting a Young Sun-like Star and Future Prospects for Detecting Eclipses by Circumsecondary and Circumplanetary Disks. *Astron. J.* **143**, 72 (2012).
18. Espaillat, C. *et al.* An Observational Perspective of Transitional Disks.. In Beuther, H., Klessen, R. S., Dullemond, C. P. & Henning, T. (eds.) *Protostars and Planets VI*, 497–520 (2014).
19. Zhu, Z., *et al.* Transitional and Pre- transitional Disks: Gap Opening by Multiple Planets? *Astrophys. J.* **729**, 47 (2011).
20. Haffert, S. Y. *et al.* Two accreting protoplanets around the young star PDS 70. *Nature Astronomy* **3**, 749–754 (2019).
21. Ruíz-Rodríguez, D. *et al.* The frequency of binary star interlopers amongst transitional discs. *Mon. Not. R. Astron. Soc.* **463**, 3829–3847 (2016).
22. Newton, E. R. *et al.* TESS Hunt for Young and Maturing Exoplanets (THYME): A Planet in the 45 Myr Tucana-Horologium Association. *Astrophys. J.* **880**, L17 (2019).
23. Bate, M. R. *et al.* Observational implications of precessing protostellar discs and jets. *Mon. Not. R. Astron. Soc.* **317**, 773–781 (2000).
24. Christian, S. *et al.* A Possible Alignment Between the Orbits of Planetary Systems and their Visual Binary Companions. *Astron. J.* **163**, 207 (2022).
25. Bate, M. R. *et al.* On the diversity and statistical properties of protostellar discs. *Mon. Not. R. Astron. Soc.* **475**, 5618–5658 (2018).
26. Kuffmeier, M., Dullemond, C. P., Reissl, S. & Goicovic, F. G. Misaligned disks induced by infall. *Astron. Astrophys.* **656**, A161 (2021).
27. Casassus, S. *et al.* An inner warp in the DoAr 44 T Tauri transition disc. *Mon. Not. R. Astron. Soc.* **477**, 5104–5114 (2018).
28. Kraus, S. *et al.* A triple-star system with a misaligned and warped circumstellar disk shaped by disk tearing. *Science* **369**, 1233–1238 (2020).
29. Davies, C. L. Star-disc (mis-)alignment in Rho Oph and Upper Sco: insights from spatially resolved disc systems with K2 rotation period. *Mon. Not. R. Astron. Soc.* **484**, 1926–1935 (2019).

30. Benisty, M. *et al.* Shadows and asymmetries in the T Tauri disk HD 143006: evidence for a misaligned inner disk. *Astron. Astrophys.* **619**, A171 (2018).

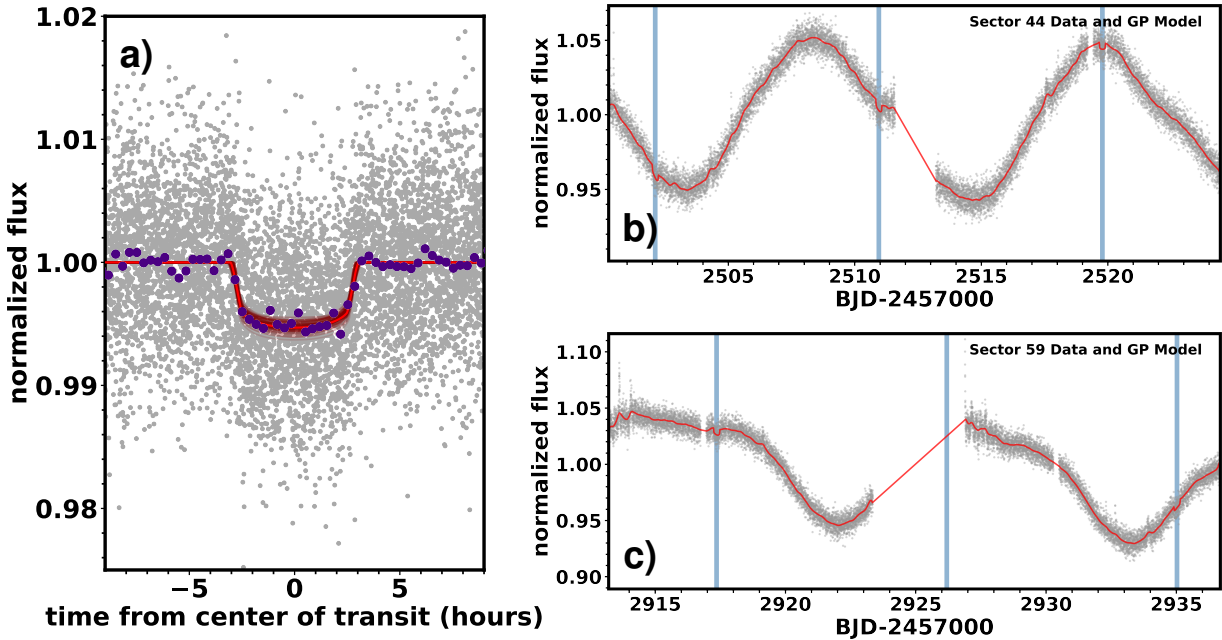


Figure 1: *TESS* light curve of IRAS 04125+2902

**a)** Phase-folded light curve from *TESS* (gray points) binned to 20-minute intervals (purple points). The uncertainty on the binned points are smaller than the size of the symbols. The best-fit transit model is shown as the bright, opaque red line with 100 model fits pulled from the posterior shown as the dark, translucent red lines. The best-fit GP model of the stellar variability was removed from the data and model. **b & c)** Representative sectors of the *TESS* light curve (gray points) with the best-fit GP model (red line). Blue regions indicate transits, which are visible by eye in most cases. In total, across the six sectors, *TESS* observed 17 transits.

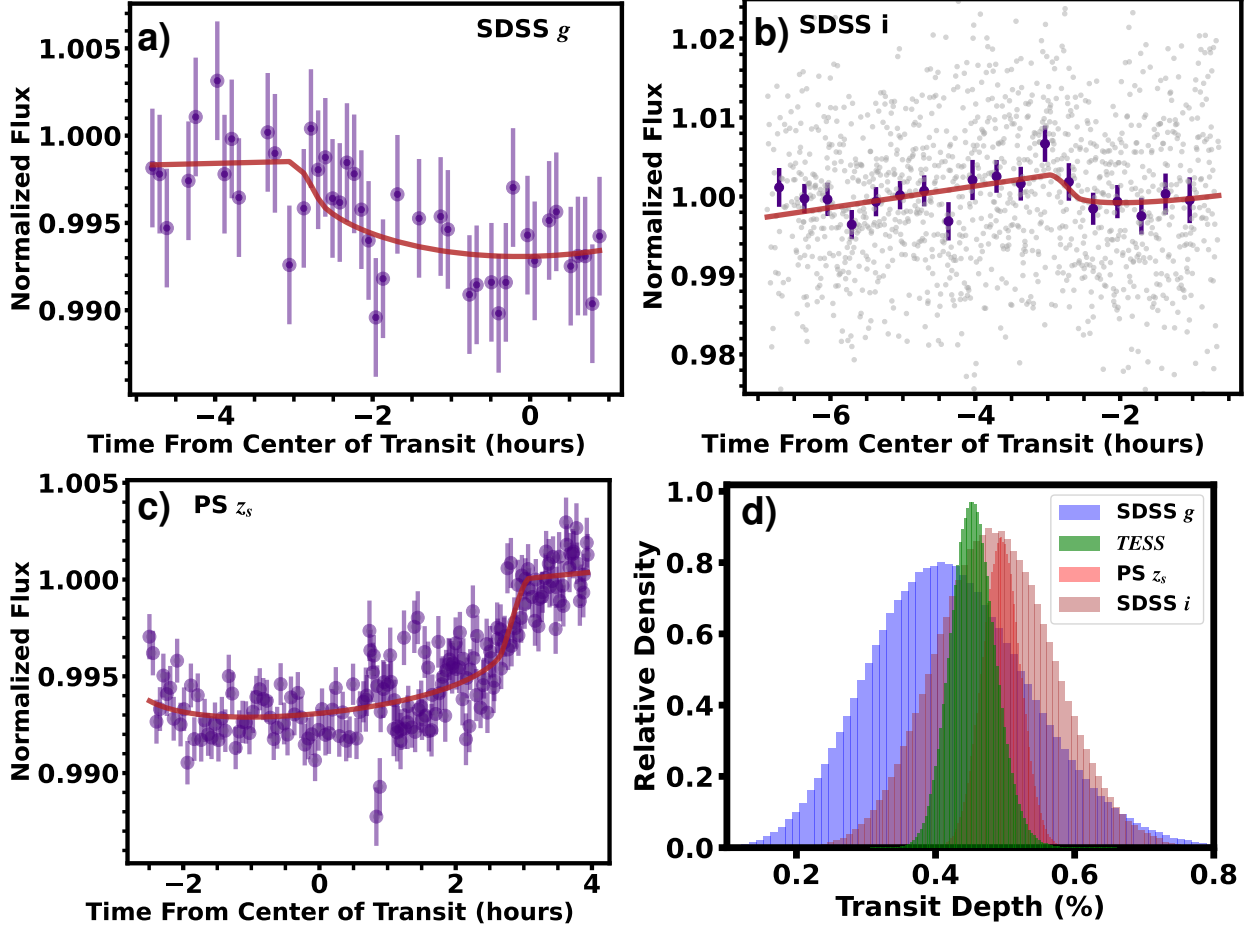


Figure 2: Ground-based transit observations of IRAS 04125+2902

**a, b, & c)** Ground-based follow-up transits observed by LCO. Light curves of the same filter have been combined (two PS  $z_s$  and two simultaneous SDSS  $i$ ). Binned points are shown for SDSS  $i$  for clarity. Error bars are the  $1\sigma$  uncertainties of the measurement for the SDSS  $g$  (**a**) and PS  $z_s$  (**c**) data and the standard error on the binned flux for SDSS  $i$  (**b**) data. The models (red lines) are the best-fit transit model with a linear trend. **d)** Transit depth posterior from each of the four wavelengths. All calculated transit depths shown in Extended Table 1.

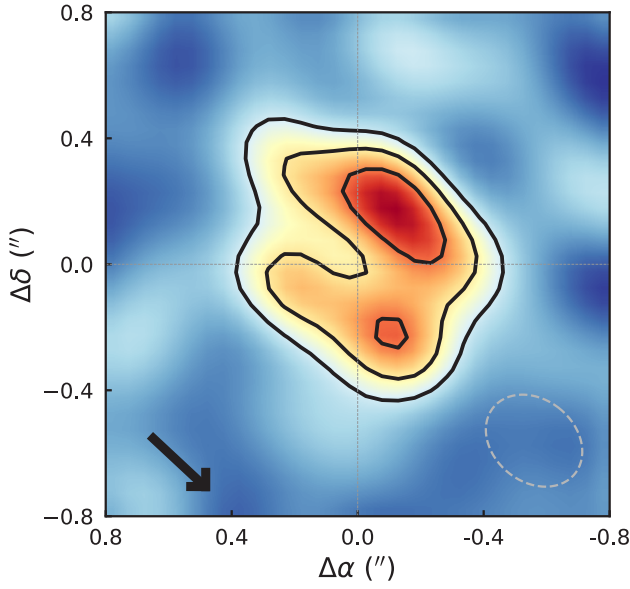


Figure 3: SMA observations of the protoplanetary disk

Archival SMA 880  $\mu\text{m}$  continuum emission of IRAS 04125+2902<sup>3</sup>. The image is centered on the estimated disk center and is scaled so that reddest color is equal to the peak flux density. Contours at  $2\sigma$ ,  $4\sigma$ , and  $6\sigma$  (3.1, 5.3, and 8.0 mJy) are shown by the black solid lines. The synthesized beam is illustrated by the dashed gray ellipse drawn in the lower right corner. The black arrow points in the direction of the binary companion. The irregular shape is likely due to the resolution of the data rather than asymmetries of the disk.

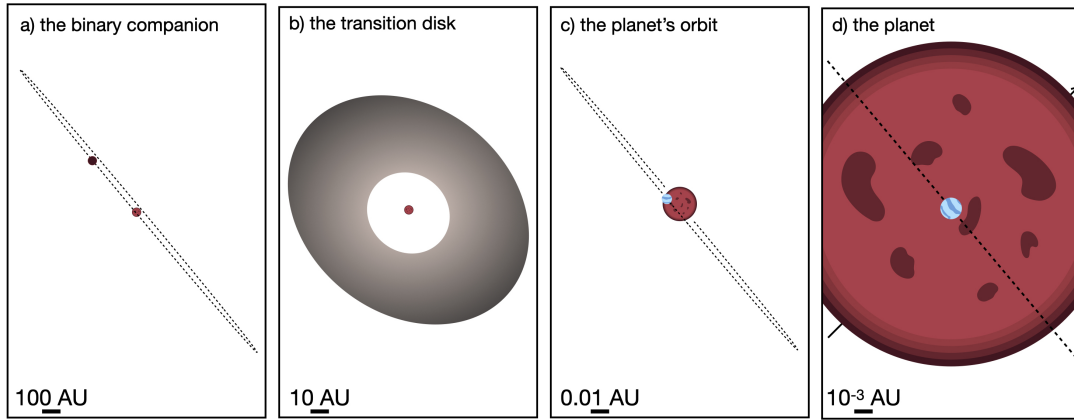


Figure 4: Illustration of the system configuration

Schematic of the system showing the stellar orbit (a), the disk (b), the planet orbit (c), and the planet (d). The scale is correct within each panel, and the inclination angle is preserved between panels. Note that the ascending node ( $\Omega$ ) is not known for the star or planet, but are drawn to match the binary.

## Methods

**TESS observation and identification of the planet:** IRAS 04125+2902 (TIC 56658270) was first observed by the Transiting Exoplanet Survey Satellite (*TESS*) in Sector 19, from 2019 Nov 28 to Dec 23. The target was re-observed by *TESS* in Sector 43 (2021 Sep 16 - Oct 11), Sector 44 (2021 Oct 12 - Nov 5), Sector 59 (2022 Nov 26 - Dec 23), Sector 70 (2023 Sep 20 - Oct 16) and Sector 71 (2023 Oct 17 - Nov 11). For Sectors 43, 44, 59, 70, and 71, the target was pre-selected for 2-minute cadence light curves produced by the Science Processing Operations Center (SPOC)<sup>31</sup>. Sector 19 was observed only in the 30-minute cadence Full Frame Images (FFIs).

As part of our survey for planets transiting stars in the youngest stellar associations, we searched the *TESS* light curves of all high-probability members of the Taurus-Auriga association<sup>4</sup>. We used a custom extraction pipeline starting from *TESS* FFIs and SPOC Simple Aperture Photometry (SAP)<sup>32</sup>. We extracted the light curves and applied our custom systematic corrections following the procedure in reference<sup>33</sup>. To briefly summarize, we started with 30x30 pixel cutouts of *TESS* FFIs. Using the calibrated pixel files, we tested a range of circular and irregular aperture shapes, adopting the one that minimized the photometric scatter and nearby-star contamination. The resulting light curves were then corrected with a linear model including a regularly-spaced B-Spline, several moments of the distribution of the spacecraft quaternion time series measurements within each exposure, the robust mean of pixels in the background of the FFI cutouts, and seven co-trending basis vectors from the SPOC Presearch Data Conditioning<sup>34,35</sup> single-band and band 3 (fast timescale) flux time series correction with the largest eigenvalues. The SPOC SAP curves were fit with a similar procedure, but with additional basis vectors and a high-pass filter on the background time series.

We searched for planets using the Notch pipeline<sup>36</sup>. From the original code, we updated the box-least squares (BLS) search to the one implemented in `astropy`<sup>37</sup>, and changed the period grid spacing used. The search recovered a signal at 8.8 days with a BLS SNR of 42. The resulting phase-folded transit showed a sharp ingress/egress with a flat bottom consistent with a planetary object.

We performed a suite of initial quality checks on the detection, including retrieval of the planet using multiple light curve pipelines<sup>38</sup>, checking depth and duration consistency with varying aperture selection and across all six sectors. Passing these checks triggered our follow-up with a suite of high-resolution imaging, multiwavelength transits, and high-resolution spectroscopy, and checking for corresponding archival data which we detail below.

The *TESS* Science Office vetting team independently identified the signal and upgraded the system to TOI-6963 on April 3 2024.

**High-Resolution Imaging:** The target has archival high-resolution imaging spanning November 2009 to November 2016. This includes deep *H*-band imaging from the Strategic Exploration of Exoplanets and Disks with Subaru (SEEDS)<sup>39</sup>, as well as *L<sub>p</sub>*-band imaging<sup>40</sup>, *K'*-band imaging,

and  $K'$ -band non-redundant aperture masking (NRM)<sup>21</sup> with NIRC2 on Keck-II.

To provide a more recent epoch, we observed IRAS 04125+2902 on 2023 Dec 5 with  $K'$ -band adaptive optics imaging using NIRC2 on Keck-II. These observations were taken, reduced, and analyzed following prior strategies optimized for identifying stellar companions to *Kepler* planet hosts<sup>41</sup>.

We summarize the resulting contrast limits from the high-resolution data in Extended Figure 6a by band and time, alongside the location of the source at three epochs based on the *Gaia* proper motions in Figure 6bc.

**Ground-based Transits:** We observed four transits of the host star with the Las Cumbres Observatory telescope network (LCO)<sup>42</sup>. These were observed with Sinistro cameras, with a pixel scale of  $0.389'' \text{ pixel}^{-1}$ . On 2023 December 9 and 18, we observed egress using the Pan-STARRS  $z_s$  filter; on 2024 January 14, we observed an egress with the Sloan  $g'$  filter; and on 2024 Jan 22, we observed ingress simultaneously with two telescopes both using the SDSS  $i'$  filter (we extracted each light curve separately). The exposure times were 300, 150, and 3 s for  $g'$ ,  $z_s$ , and  $i'$  observations, respectively. Due to the long transit duration, all were partial transits.

All images were initially reduced by the standard LCOGT BANZAI pipeline<sup>43</sup>. We tested extracting photometry from BANZAI, AstroImageJ<sup>44</sup>, and Photutils, varying sets of between 10 and 15 comparison stars, and varying aperture sizes (diameter of 1-6''). We recovered the transit with consistent depth across all methods.

**Radial Velocities of IRAS 04125+2902:** We retrieved two sets of spectra of the target taken with the Immersion Grating Infrared Spectrometer (IGRINS)<sup>45</sup> on 2015 Jan 27 and 2017 Dec 02. These observations were taken as part of a survey of young stellar objects in nearby star-forming regions<sup>78</sup>. We reduced the IGRINS spectra with the publicly available IGRINS pipeline package<sup>46</sup> and extracted RVs using the IGRINS RV code<sup>47</sup>. The RVs were consistent with no variation over a 3-year baseline.

We drew four additional RV measurements from the seventeenth APOGEE data release<sup>48</sup>. The RVs span 2019 January 20 to 2020 January 6, and are consistent with no variation over this period.

We convert the absolute RVs from APOGEE and IGRINS into a comparable relative frame by subtracting the median value of the six measurements.

We obtained six new observations of the star with the Habitable-zone Planet Finder (HPF)<sup>49,50</sup> on the 10-m Hobby-Eberly Telescope at McDonald Observatory. HPF is a high resolution ( $R \sim 55000$ ), fiber-fed<sup>51</sup>, stabilized<sup>52</sup> spectrograph covering  $8100 - 12700 \text{ \AA}$ . HPF has a laser frequency comb (LFC) to achieve extremely high quality wavelength calibration, exhibiting  $\sim 20 \text{ cm s}^{-1}$  instrumental calibration precision<sup>53</sup>.

Each HPF observation was composed of three sequential 600-s exposures to increase signal and average over high-frequency, oscillation-driven stellar RV variation. To minimize the effect of stellar activity-driven RV noise, we scheduled observations within one stellar rotation (11 days) while sampling at orbital phases of maximum velocity expected from the planet. We bracketed each observation with LFC exposures to monitor the instrumental velocity drift.

The HPF data were reduced using the HxRGproc toolbox<sup>54,55</sup>. We corrected the derived wavelength solution for barycentric motion at the flux-weighted exposure midpoint using `barycorrpy`<sup>56</sup>. We measured RVs using broadening functions<sup>57</sup> computed using the `saphires` Python package<sup>58,59</sup>, which compares each individual spectrum to a template. We used an empirical template of the spectrum generated by stacking all HPF observations, and measured the RV by fitting a Gaussian to the combined broadening function for each HPF exposure and binned the three RVs comprising each observation. We repeated this procedure using a Phoenix model spectrum<sup>60</sup> to provide RVs on the same scale as the IGRINS and APOGEE RVs, because comparison to an empirical template offers more precise, but only relative RVs.

All RVs are summarized in Extended Table 3 and Extended Figure 1.

**Host star properties:** Star-forming regions near the Sun are generally Solar or slightly sub-Solar metallicity<sup>61</sup>. The Taurus-Auriga region is also consistent with Solar metallicity<sup>62</sup>, so we assume Solar metallicity for all analyses of the host-star properties.

We determined  $R_*$ ,  $L_*$ , and  $T_{\text{eff}}$  by simultaneously fitting the available photometry and the archival optical spectrum<sup>63</sup>. This approach has yielded radii accurate to 4-6% on extincted pre-main-sequence stars<sup>64,65</sup>. To summarize, we compared a grid of flux-calibrated optical and near-infrared spectra<sup>66,67</sup> to the available photometry and observed spectrum. The templates include young unreddened young stars from nearby moving groups<sup>68</sup>. We used this grid because the flux-calibration is good to 2-4%<sup>66</sup> and the optical data uses the same instrument as the archival optical spectrum (SNIFS;<sup>69</sup>). We used BT-SETTL atmospheric models<sup>70</sup> to fill in gaps in the spectra (e.g., beyond  $2.3\mu\text{m}$ ). In total we fit for five parameters; the choice of template, extinction ( $A_V$ ), the model selection, and two nuisance parameters that capture imperfections in the flux calibration of SNIFS. We excluded photometry past  $8\mu\text{m}$ , which includes emission from the disk. Data blueward of this was consistent with the photosphere both in our analysis and prior fits of the SED including a disk model<sup>3</sup>. After accounting for stellar variability, the best-fit template reproduced the spectrum extremely well ( $\chi^2_\nu = 1.1$ , Extended Figure 2).

We estimated the bolometric flux ( $F_{\text{bol}}$ ) from the integrated spectrum, the luminosity from  $F_{\text{bol}}$  and the *Gaia* parallax, and  $R_*$  from the Stefan-Boltzmann relation. The final fit yielded  $T_{\text{eff}}=3912 \pm 72$  K,  $L_* = 0.466 \pm 0.041L_\odot$ ,  $A_V = 2.71 \pm 0.20$ , and  $R_* = 1.48 \pm 0.07R_\odot$ . We obtain another estimate of  $R_*$  from the scale factor between the BT-SETTL model and the photometry (equal to  $R_*^2/\text{distance}^2$ ), which yields a smaller but consistent  $R_* = 1.39 \pm 0.08R_\odot$ .

We performed a similar SED fit to the companion and provide the resulting parameters in

Table 5.

The template grid is mostly main-sequence stars, while our target is pre-main-sequence. Prior work has found this has a weak impact on the final parameters<sup>64</sup>. We further tested this by repeating our fit of the primary star using a grid of unreddened optical spectra of T-Tauri stars<sup>63</sup>. This yielded fit parameters within  $0.5\sigma$  of those above. The fit using T-Tauri stars was worse ( $\chi^2_\nu = 1.6$ ) and the grid lacked empirical NIR spectra, so this fit was only used to confirm that gravity has a weak impact on our SED analysis.

The analysis above does not consider the impact of spots on the final stellar parameters, which may be significant for such a young star. We repeated the analysis above but replacing the templates with BT-SETTL models and using a two-temperature fit<sup>71,72</sup>. This added two additional parameters: the spot coverage fraction ( $f_S$ ) and the difference between the surface and spot temperature ( $\Delta T$ ). These parameters were limited to  $0 < f_S < 1$  and  $\Delta T < 1000$  K. The latter limit is set by the most extreme spot temperatures observed in similar T-Tauri stars<sup>73,74</sup>. We restricted our models  $\log g = 4.0$  based on our derived  $M_*$  and  $R_*$ , but adopting 3.5 or 4.5 had no impact on the result. The temperature difference was poorly constrained, but our fit ruled out large spot coverage fractions ( $f_S > 0.4$ ) except when the spots are warm ( $\Delta T < 250$  K). Cooler spots change the SED shape or imprint molecular lines that would be visible in the optical spectrum when  $f_S$  is large<sup>75</sup>. As above, we calculate a radius from the scale factor, giving us similar radii to our prior analyses ( $R_* = 1.45 \pm 0.10 R_\odot$ ) and a slightly warmer but consistent temperature ( $T_{\text{eff}} = 4080 \pm 95$  K). We adopt this more conservative  $T_{\text{eff}}$  and  $R_*$  for further analyses of the host star.

To estimate  $M_*$  and age, we compared photometry and distance to the PARSECv1.2S<sup>5</sup> and BHAC15<sup>76</sup> model grids within an MCMC framework<sup>77</sup>. As with the SED fit, we excluded photometry past  $8\mu\text{m}$ . The free parameters were the stellar mass ( $M_*$ ), age, extinction ( $A_V$ ), and underestimated uncertainty ( $f$ ). We placed a Gaussian prior on  $A_V$  based on a fit of the optical spectrum with a stellar template, but other parameters evolved under uniform priors. The PARSEC models yielded a  $M_* = 0.70 \pm 0.04 M_\odot$  and an age of  $3.3^{+0.6}_{-0.5}$  Myr, while BHAC15 gave  $M = 0.67 \pm 0.05 M_\odot$  and an age of  $3.1 \pm 0.4$  Myr. The model fits also provided estimates for  $T_{\text{eff}}$  and  $R_*$  of  $3950 \pm 60$  K and  $1.6 \pm 0.1 R_\odot$  from PARSEC and  $4037 \pm 90$  K and  $1.47 \pm 0.08 R_\odot$  from BHAC15. These parameters are consistent with our SED fit above, and the ages consistent with the parent Taurus-Auriga sub-group<sup>4</sup>. We adopted the PARSEC results because of a lower  $\chi^2$  in the comparison.

We tried fitting the primary and 4'' companion simultaneously, assuming the same age. The fit was largely unchanged ( $3.6 \pm 0.6$  Myr) from the primary-only fit. This provided an mass estimate  $M = 0.17 \pm 0.04 M_\odot$  for the companion we use in our binary orbit fit. We summarize the host and companion stellar properties in Extended Table 5.

Our stellar parameters are consistent to prior independent measurements<sup>3,63</sup>, including  $T_{\text{eff}}$  from analyses of the APOGEE<sup>48</sup> spectra and both  $T_{\text{eff}}$  and  $\log(g)$  from analyses of the IGRINS spectra<sup>78</sup>. These analyses have also found the star to have little or no veiling in the optical or near-

infrared. Since these parameters were broadly consistent, we did not perform a new analysis of the IGRINS and APOGEE spectra.

Prior analysis of this target noted a  $U$ -band excess, suggestive of an accretion rate of  $3_{-2}^{+6} \times 10^{-10} M_{\odot} \text{ yr}^{-1}$ <sup>3</sup>, consistent with what is seen in other transitional disks<sup>79</sup>. We detected a weak Pa $\gamma$  line in the HPF spectra, which we combine with  $L_{\text{acc}} - L_{\text{line}}$  relations<sup>80</sup> to estimate an accretion rate of  $\simeq 10^{-9} M_{\odot} \text{ yr}^{-1}$ . We observe no significant Brackett or Paschen emission lines in the IGRINS data. Combined with the relatively low H $\alpha$  emission<sup>81</sup>, the star is likely undergoing variable and/or weak accretion.

**Star-planet alignment:** We estimated the inclination of the host star ( $i_*$ ) using the combination of the stellar rotation period ( $P_{\text{rot}}$ ), rotational broadening ( $V \sin(i_*)$ ), and the stellar radius ( $R_*$ ).

We measured  $P_{\text{rot}}$  by running a Generalized Lomb Scargle (GLS) periodogram on the *TESS* light curves. We used the simple-aperture photometry (SAP) fluxes, which we median-normalized to unity within a given sector, then stitched all sectors together. For the  $P_{\text{rot}}$  uncertainty, we used the standard deviation in  $P_{\text{rot}}$  determinations between sectors and the stitched curve. We find a final rotation period  $P_{\text{rot}} = 11.31 \pm 0.06$  days.

To estimate rotational broadening ( $V \sin(i_*)$ ) we cross-correlated the IGRINS spectra with artificially broadened IGRINS spectra of slowly-rotating stars with similar  $T_{\text{eff}}$  to the host star. The adopted  $V \sin(i_*)$  was the broadening that gave the maximum cross-correlation. As with prior work<sup>82</sup>, we focused on spectral regions containing the CO bands because they are insensitive to the effect of magnetic fields<sup>83</sup>. To estimate uncertainties, we repeated this process over multiple orders and with multiple templates, yielding a  $V \sin(i_*)$  of  $7.1 \pm 0.5 \text{ km s}^{-1}$ . We also tested using PHOENIX atmosphere models, which let us explore the effect of lowering the surface gravity, and obtained a consistent  $6.8 \text{ km s}^{-1}$ . Our estimate was also consistent with earlier determinations which included direct modelling of small-scale magnetic fields<sup>78</sup>.

Using the  $R_*$  and  $P_{\text{rot}}$  values above gave an equatorial velocity of  $6.6 \pm 0.3 \text{ km s}^{-1}$ , which we combined with our  $V \sin(i_*)$  estimate to set limits on  $i_*$ . Our method for computing  $i_*$  accounts for statistical complications in estimating  $i_*$  laid out in prior studies<sup>84</sup>, including corrections for the effective barrier at  $\sin(i_*) = 1$ . Our analysis yielded a lower limit on  $i_* > 78^\circ$  at  $1\sigma$  and  $> 68^\circ$  at  $2\sigma$ . The resulting inclination is consistent with that of the transiting planet. Despite the inclinations agreeing, the ascending nodes ( $\Omega$ , the sky-projected angles) are unconstrained, and therefore the host star and planet are not necessarily truly aligned.

**Star-binary alignment:** *Gaia* detected a star  $\simeq 4''$  away (TIC 56658273), corresponding to a sky-projected separation of 635 AU. To estimate the probability that this star is a random alignment versus a bound companion, we used the BinProb tool within Comove<sup>85</sup>. To briefly summarize, BinProb compares the projected separation, Gaia contrast, relative proper motion, and parallax of a simulated binary population<sup>86</sup> orbiting IRAS 04125+2902 to the values of the empirical field population of nearby sources from *Gaia* (<1 degree). It uses a kernel density estimator to smooth

both populations across phase space and then computes the probability from the relative amplitudes of their probability density functions. This gave a probability that TIC 56658273 is a bound binary companion of  $P_{bin} > 99.99\%$ .

We recovered TIC 56658273 in the three epochs from NIRC2/Keck. There are not enough stars in the field of view to establish an external reference frame. Instead, we measured the relative astrometry between the target and companion by fitting the PSFs with an empirical template built from other images taken in the same night<sup>41</sup>. We applied a  $-0.062$  deg offset to the NIRC2 position angles to put them on the same scale as the *Gaia* astrometry. We summarize the resulting measurements in Extended Table 2.

A wide binary companion can explain the presence of a misaligned disk depending on the binary orbit<sup>87</sup>. To investigate this, we fit the orbit of TIC 56658273 relative to the system using `lofti`<sup>88</sup>. `lofti` uses the orbit fitting rejection sampling algorithm of OFTI<sup>89</sup> with relative *Gaia* proper motions and Keck astrometry as observational constraints.

Extended Figure 5b shows posterior distributions for the semi-major axis, period, and inclination resulting from our binary orbit fit. Due to the astrometric points covering only a small fraction of the orbit, the eccentricity is unconstrained<sup>90</sup>. We find the companion’s orbital inclination ( $i_c$ ) is  $94.5^{+10.9}_{-4.7}$  degrees. This is consistent with the edge-on orbit of the star-planet system (within  $1\sigma$ ).

Both the *Gaia* and Keck astrometry are consistent with purely radial motion, although most of the orbital information came from the difference in *Gaia* proper motions. However, the *Gaia*-only fit yielded  $i_c = 95 \pm 20$  degrees, highlighting the need for the NIRC2 astrometry to refine the fit.

**Disk-star alignment and disk properties:** IRAS 04125+2902 is known to harbor a transitional disk, as evident from the SED peak at  $\simeq 100\mu\text{m}$  and a central hole seen in submm/mm imaging<sup>3</sup>.

To confirm a previous estimate of disk inclination ( $i_d$ )<sup>3</sup>, we reanalyzed the Submillimeter Array (SMA) data. We fit a simple elliptical Gaussian to the visibility data with the `uvmodelfit` task in CASA (version 6.5.6.22). Using CASA’s `importuvfits` task, we converted the SMA observations in UVFITS format to a CASA visibility data set. The `uvmodelfit` elliptical Gaussian model has six free parameters: integrated flux density ( $F_{\text{cont}}$ ), FWHM along the major axis ( $a$ ), aspect ratio of the axes ( $r$ ), position angle (PA), right ascension offset from the phase center ( $\Delta\alpha$ ), and declination offset from the phase center ( $\Delta\delta$ ). We scaled the uncertainties on the fitted parameters by the square root of the reduced  $\chi^2$  value of the fit. We found  $r = 0.856 \pm 0.077$ , which implies an outer disk inclination  $31 \pm 12^\circ$ , consistent with the prior determination of  $\lesssim 30^\circ$ <sup>3</sup>. We show the image extracted from the visibilities in Figure 3. The disk inclination disagrees with the star-planet-binary system by  $\sim 4\sigma$ .

We calculate the disk gas mass from sub-mm/mm flux density under the assumption of optically thin and isothermal dust emission<sup>91</sup>. This method has been employed for large-scale ALMA

surveys of nearby disk populations<sup>92</sup> by assuming a dust grain opacity ( $\kappa_\nu$ ) of  $10 \text{ cm}^2 \text{ g}^{-1}$  at 1000 GHz and using an opacity power-law index of  $\beta_d = 1.0$ <sup>93</sup>. Using the *Gaia* parallax, we find  $M_{\text{dust}} = 10.6 \pm 0.3 M_\oplus$ , or  $M_{\text{gas}} = 0.00318 \pm 0.0009 M_\odot$  assuming a gas-to-dust mass ratio of 100. This is lower than previous analyses of the disk, which found a dust mass of  $15.3 M_\oplus$  ( $M_{\text{gas}} = 0.005 M_\odot$ )<sup>94</sup> and  $16.65 - 23.31 M_\oplus$  (from  $M_{\text{gas}} = 0.005 - 0.007 M_\odot$ )<sup>3</sup>. All three fits assumed the same gas-to-dust mass ratio but used different distances and wavelengths for converting from the continuum flux, causing discrepancies in the derived masses.

## Planet Properties

**Transit analysis:** For the transit, we use our FFI-extracted light curve for Sector 19 and the 2-minute systematic-corrected SPOC PDPSAP light curves for Sectors 43, 44, 59, 70, and 71. We remove one transit in Sector 43 (expected  $T_0 \simeq 2459484.5 \text{ BJD\_TBD}$ ) as the transit occurs close to the *TESS* data edge. We remove a flare at  $\sim 2459519.95 \text{ BJD\_TBD}$ , which marginally interrupts the egress of a transit in Sector 44 (expected  $T_0 \simeq 2459519.8 \text{ BJD\_TBD}$ ).

We fit the systematics-corrected *TESS* photometry using MISTTBORN (MCMC Interface for Synthesis of Transits, Tomography, Binaries, and Others of a Relevant Nature) code<sup>95,96</sup>. MISTTBORN utilizes BATMAN<sup>97</sup> to generate the light curve models, emcee<sup>77</sup> to explore the parameter space, and celerite<sup>98</sup> to model the stellar variability with a Gaussian Process (GP).

We fit 10 parameters in total. Five are the common transit parameters: time of periastron ( $T_0$ ), planet orbital period ( $P$ ), planet-to-star radius ratio ( $R_p/R_*$ ), impact parameter ( $b$ ), and stellar density ( $\rho_*$ ). We also fit two quadratic limb darkening coefficients ( $q_1$  and  $q_2$ ) following the triangular sampling prescription<sup>99</sup>.

The last three parameters were used to model the GP in the celerite code. We used a stochastically-driven damped simple harmonic oscillator (SHO) to model the stellar variability. SHOs have been proposed as ideal for stellar variability modeling<sup>98</sup>, and have been used widely for *TESS* photometry of young stars<sup>65,100</sup>. The GP consisted of three parameters: the natural logarithm of the GP period ( $\ln(P)$ ), the natural logarithm of the GP amplitude ( $\ln(\text{amp})$ ), and a quality factor ( $\ln(Q)$ ).

We show the best-fit parameters with uncertainties in Extended Table 4. We also show the phase-folded light curve with the best-fit and sample-fit model transits and representative sectors with the GP fit in Figure 1 and representative transits in Extended Figure 3. We show how the planet compares in period and radius space to the set of known, young (< 700 Myr) transiting planets in Extended Figure 4.

While we did not explicitly fit for eccentricity, we can gain some constraints by comparing the transit-fit stellar density to the estimated stellar density from our SED fit. The transit-fit  $\rho_*$  is sensitive to the transit duration, so any disagreement between the two values would suggest an eccentric planet<sup>102</sup>. The transit fit yielded a density of  $\rho_* = 0.26^{+0.05}_{-0.09} \rho_\odot$  and SED/model fit yielded  $\rho_* = 0.23 \pm 0.05 \rho_\odot$ , in agreement with our assumed circular-orbit transit-fit. Alternatively, if we

assume the orbit is circular, this provides additional confirmation of our stellar parameters.

We fit the ground-based transits using the BATMAN model as above, but replaced the GP with a linear model to handle out-of-transit variations, updated the limb-darkening values to the relevant wavelength, and locked other parameters to the fit of the *TESS* data excluding  $R_P/R_*$  and  $T_0$ . The variability model coefficients,  $a$  and  $b$ , were fit by removing a correction of the form  $f(t) = a + b \times (t - \min(t))$ . We simultaneously fit transits observed in the same filter. The resulting transit fits are shown in Figure 2, and the inferred transit parameters are shown in Extended Table 1. The estimated transit depth was consistent across all observed wavelengths, and all agreed with the *TESS* depth to  $< 1\sigma$ .

**TTV analysis:** Using the same light curves as above, we searched for transit timing variations (TTVs) of the system. TTVs may suggest the presence of another planet and large TTVs can bias the inferred transit properties. To this end, we fit each transit separately using the BATMAN model, with the exception of the transit near the *TESS* data edge, locking all parameters to the *TESS* fit, except the transit midpoint. For stellar variability, we model the region around each transit with a Gaussian process (GP) from `celerite`, utilizing the simple harmonic oscillator (SHO) kernel as above. We ran the MCMC using 30 walkers for 10,000 steps including a burn-in of 2,000 steps (for each transit). Transit variations were calculated by comparing observed with calculated (O-C) transit midpoints. We find that fourteen of the sixteen (88%) transits in the analysis agreed with the predicted period (O-C of zero) within  $1\sigma$ , with the remaining two transits being  $1.9\sigma$  (27.0 minutes) and  $2.3\sigma$  (20.6 minutes) off, suggesting no significant TTVs are present and our parameters are not biased by assuming a linear ephemeris.

**RV analysis:** We fit the relative RVs from HPF. Fitting just the HPF data allowed us to minimize the effects of long-term variations in the stellar signal. We fit only three parameters; the planet's semi-amplitude ( $K$ ), a velocity offset ( $\gamma$ ), and the jitter ( $\sigma_J$ ). All parameters evolved under uniform priors with only physical limits. The jitter term is added in quadrature with the measurement uncertainties. Other parameters were locked to the results from the transit and we assumed zero eccentricity. Using  $K$ , we fit for the mass and find an upper limit on the mass of IRAS 04125+2902 b of  $0.3M_J$  (95%) with a jitter of  $60 \text{ m s}^{-1}$ . The fitted mass posterior agrees with the distribution of planets of similar radii. However, the best-fit mass suggests the planet is low density compared to other large planets with mass measurements, and models predict young super-Earths and mini-Neptunes should be similar in radius to IRAS 04125+2902 b<sup>103</sup>.

The APOGEE and IGRINS data agree with the fitted signal using just HPF, despite the long baseline between observations. This holds even using the (less precise) absolute velocities, confirming that our signal has no long-term trend and is planetary-mass. We do not include the archival velocities in our mass limit since there are too few points to model any zero-point offsets between the instruments. Allowing for more parameters to float (eg, eccentricity) or allowing for more complex jitter terms increased the mass limit, but under any condition we find  $M_p < 2M_J$  (95%).

**False positive analysis:** We consider each false-positive scenario individually below.

*Transit signal originates from instrumental artifacts:* The transit is recovered in both *TESS* and ground-based data across different sites, filters, and instruments.

*Transit signal originates from stellar variability:* While the stellar variability amplitude is large (1-10%; Figure 1), the signal is spread over  $\simeq 11.3$  days; in some sectors, the stellar signal is weaker than the planet signal over the 6-hour transit duration. The stellar variability profile evolves between *TESS* sectors (Figure 1), yet the transit signal remains constant. Despite some stellar variability signals mimicking transit-like depths and durations, these signals are not periodic. Finally, the transit is recovered from ground-based data at multiple wavelengths, while stellar signals will depend on wavelength.

*Transit signal is from a background or foreground star:* Based on the proper motions from *Gaia*, the host star has moved by  $\sim 305$  mas (in the *Gaia* frame) over the 14 years spanned by the high-resolution data. This is more than the inner working angle of the Keck/NIRC2 image ( $\sim 100$  mas). As a result, a background/foreground star that was undetected in one set of Keck/NIRC2 observations because it happen to be behind or in front of the target would be visible in later observations. We show the locations of IRAS 04125+2902 at each of the imaging epochs in Extended Figure 6. This rules out any background/foreground source with  $\Delta K < 5$  mag.

We can use the transit depth and shape to set limits on the brightness of sources that can reproduce the transit by considering the depth and duration of the largest possible companion. From this, the ratio of the ingress or egress duration to the duration from first to third contact (start of ingress to start of egress) limits the radius ratio of the transit source regardless of any diluting flux<sup>33</sup>. This calculation suggests if the transit signal comes from another star, it must be  $\Delta T \leq 1.7$  mag fainter ( $T \leq 14.5$  mag) at 99% confidence. This is far brighter than the limits set by the imaging.

*IRAS 04125+2902 b is an eclipsing binary or brown dwarf:* A basic fit to the RVs rules out anything with mass  $> 0.3M_J$ . Even under pessimistic assumptions about the eccentricity and stellar variability, all brown dwarf masses ( $> 13M_J$ ) are easily rejected. Further, the Sonora Bobcat models<sup>104</sup> predict an object with a brown-dwarf mass ( $\sim 13 M_J$ ) at this age would be  $\sim 2.0 R_J$ , inconsistent with our fitted radius ( $\simeq 1R_J$ ).

*Transit signal is from an eclipsing binary bound to IRAS 04125+2902:* To set additional limits on bound companions, we combine the high resolution images, RVs, and *Gaia* imaging using MOLUSC (Multi-Observational Limits on Unseen Stellar Companions)<sup>105</sup>. MOLUSC generates synthetic companions and compares them to the observational data. Since we are only interested in companions that could reproduce the transit, we reject any companion that would not land within the photometric aperture used to recover the ground-based transits ( $2.7''$ ). This also rules out the bound companion ( $4''$ ) and any nearby sources detected in *Gaia*. MOLUSC generated 1,000,000 sample stars and  $\sim 98.4\%$  were rejected.

The remaining companions consistent with the observational data generally have small mass ratios ( $q < 0.06$ ) with long orbital periods ( $\log_{10}(P/\text{days}) = 6.31^{+1.46}_{-1.91}$ ). Applying the brightness constraints above removes all but 800 companions (0.08%). The remaining binaries are all  $\Delta J < 1.5$ ; such systems would appear as a second set of lines in our IGRINS or HPF spectra (SNR>100 per epoch) and as an elevated position on the color-magnitude diagram, neither of which were detected.

We can set additional limits using the multi-wavelength ground-based follow-up. If the transit signal were from another star, the depth would vary between bands due to changes in the relative flux contribution with wavelength<sup>85</sup>. Taking the 95th percentile of depths, we set limits on color combinations from  $g$  to  $z$ . The strongest are in  $g - T$ , which limit the true host to, at most, 0.67 mag redder than the target. As with the depth and duration constraints, allowed companions would all be detected in our suite of other follow up.

*The transit signal is a persistent flux dip or transient dipper:* Many disk-bearing young stellar objects show ‘dips’ in their light curves, commonly attributed to dust or gas near the co-rotation radius<sup>106</sup>. The overwhelming majority of these objects exhibit light curve morphology and quasi-periodicity inconsistent with a planet on a Keplerian orbit. However, PTFO 8-8695 exhibits light curve dips that were originally attributed to a planet<sup>107</sup> before it was found to be a transient dipper<sup>108</sup>. At least five other systems exhibit similar behavior<sup>109</sup>.

We can reject this scenario by comparing the light curve behavior. PTFO 8-8695 and its brethren are not truly periodic, showing both long-term variations in the dip timing and many events not happening at all<sup>110</sup>. Depths and durations from dippers (including PTFO 8-8695) vary by a factor of 2-3 over 1-2 month windows<sup>111,112</sup>. None of these systems show a flat bottom and sharp ingress/egress, the hallmarks of non-grazing planetary transits.

To test for consistency in depth and transit shape, we fit individual transits of IRAS 04125+2902 b, locking  $P$ ,  $T_0$ , and limb-darkening parameters, but allowing  $R_P/R_*$  and  $a/R_*$  to vary alongside a Matern GP kernel to handle the stellar variability. Overall, 94% of the  $R_P/R_*$  results and 100% of the  $a/R_*$  are within  $2\sigma$  of one another, suggesting a consistent transit shape across four years of data.

**Data Availability** We provide all reduced light curves and spectra as source data products to the manuscript and in a GitHub repository: [https://github.com/madysonb/discovery\\_resources](https://github.com/madysonb/discovery_resources).

**Code availability** We provide access to a GitHub repository including all code created for the analysis of this project that is not already publicly available. [https://github.com/madysonb/discovery\\_resources](https://github.com/madysonb/discovery_resources)

31. Jenkins, J. M. *et al.* The TESS science processing operations center. In *Proc. SPIE, vol. 9913 of Society of Photo-Optical Instrumentation Engineers (SPIE) Conference Series*, 99133E (2016).

32. Twicken, J. D. *et al.* Photometric analysis in the Kepler Science Operations Center pipeline. In Radziwill, N. M. & Bridger, A. (eds.) *Software and Cyberinfrastructure for Astronomy*, vol. 7740 of *Society of Photo-Optical Instrumentation Engineers (SPIE) Conference Series*, 774023 (2010).
33. Vanderburg, A. *et al.* TESS Spots a Compact System of Super-Earths around the Naked-eye Star HR 858. *Astrophys. J.* **881**, L19 (2019).
34. Stumpe, M. C. *et al.* Kepler Presearch Data Conditioning I - Architecture and Algorithms for Error Correction in Kepler Light Curves. *Publ. Astron. Soc. Pacif.* **124**, 985-999 (2012).
35. Smith, J. C. *et al.* Kepler Presearch Data Conditioning II - A Bayesian Approach to Systematic Error Correction. *Publ. Astron. Soc. Pacif.* **124**, 1000 (2012).
36. Rizzuto, A. C., *et al.* Zodiacial Exoplanets in Time (ZEIT). V. A Uniform Search for Transiting Planets in Young Clusters Observed by K2. *Astron. J.* **154**, 224 (2017).
37. Astropy Collaboration *et al.* The Astropy Project: Building an Open-science Project and Status of the v2.0 Core Package. *The Astropy Project: Building an Open-science Project and Status of the v2.0 Core Package* **156**, 123 (2018).
38. Hattori, S. *et al.* The unpopular Package: a Data-driven Approach to De-trend TESS Full Frame Image Light Curves. *arXiv e-prints* arXiv:2106.15063 (2021).
39. Uyama, T. *et al.* The SEEDS High-Contrast Imaging Survey of Exoplanets Around Young Stellar Objects. *Astron. J.* **153**, 106 (2017).
40. Wallace, A. L. *et al.* High-resolution survey for planetary companions to young stars in the Taurus molecular cloud. *Mon. Not. R. Astron. Soc.* **498**, 1382-1396 (2020).
41. Kraus, A. L., *et al.* The Impact of Stellar Multiplicity on Planetary Systems. I. The Ruinous Influence of Close Binary Companions. *Astron. J.* **152**, 8 (2016).
42. Brown, T. M. *et al.* Las Cumbres Observatory Global Telescope Network. *Publ. Astron. Soc. Pacif.* **125**, 1031 (2013).
43. McCully, C. *et al.* Real-time processing of the imaging data from the network of Las Cumbres Observatory Telescopes using BANZAI. In *Software and Cyberinfrastructure for Astronomy V*, vol. 10707 of *Society of Photo-Optical Instrumentation Engineers (SPIE) Conference Series* 107070K (2018).
44. Collins, K. A., *et al.* AstroImageJ: Image Processing and Photometric Extraction for Ultra-precise Astronomical Light Curves. *Astron. J.* **153**, 77 (2017).
45. Park, C. *et al.* Design and early performance of IGRINS (Immersion Grating Infrared Spectrometer). In *Society of Photo-Optical Instrumentation Engineers (SPIE) Conference Series*, vol. 9147 of *Society of Photo-Optical Instrumentation Engineers (SPIE) Conference Series*, 1 (2014).

46. Lee, J.-J., Gullikson, K. & Kaplan, K. igrins/plp 2.2.0 (2017).
47. Stahl, A. G. *et al.* IGRINS RV: A Precision Radial Velocity Pipeline for IGRINS Using Modified Forward Modeling in the Near-infrared. *Astron. J.* **161**, 283 (2021).
48. Abdurro'uf *et al.* The Seventeenth Data Release of the Sloan Digital Sky Surveys: Complete Release of MaNGA, MaStar, and APOGEE-2 Data. *Astrophys. J. Suppl.* **259**, 35 (2022).
49. Mahadevan, S. *et al.* The habitable zone planet finder: a proposed high-resolution NIR spectrograph for the Hobby Eberly Telescope to discover low-mass exoplanets around M dwarfs. *In Society of Photo-Optical Instrumentation Engineers (SPIE) Conference Series*, vol. 7735 of *Society of Photo-Optical Instrumentation Engineers (SPIE) Conference Series*(2010).
50. Mahadevan, S. *et al.* The Habitable-zone Planet Finder: A status update on the development of a stabilized fiber-fed near-infrared spectrograph for the Hobby-Eberly telescope. *In Ramsay, S. K., McLean, I. S. & Takami, H. (eds.) Ground-based and Airborne Instrumentation for Astronomy V*, vol. 9147 of *Society of Photo-Optical Instrumentation Engineers (SPIE) Conference Series*, 91471G (2014).
51. Kanodia, S. *et al.* Overview of the spectrometer optical fiber feed for the habitable-zone planet finder. *n Evans, C. J., Simard, L. & Takami, H. (eds.) Ground-based and Airborne Instrumentation for Astronomy VII*, vol. 10702 of *Society of Photo-Optical Instrumentation Engineers (SPIE) Conference Series*, 107026Q (2018).
52. Stefansson, G. *et al.* A Versatile Technique to Enable Sub-milli-Kelvin Instrument Stability for Precise Radial Velocity Measurements: Tests with the Habitable-zone Planet Finder. *Astrophys. J.* **833**, 175 (2016).
53. Metcalf, A. J. *et al.* Stellar spectroscopy in the near-infrared with a laser frequency comb. *Optica* **6**, 233 (2019).
54. Ninan, J. P. *et al.* The Habitable-Zone Planet Finder: improved flux image generation algorithms for H2RG up-the-ramp dat. *In Holland, A. D. & Beletic, J. (eds.) High Energy, Optical, and Infrared Detectors for Astronomy VIII*, vol. 10709 of *Society of Photo-Optical Instrumentation Engineers (SPIE) Conference Series*, 107092U (2018).
55. Kaplan, K. F. *et al.* The Algorithms Behind the HPF and NEID Pipeline. *n Teuben, P. J., Pound, M. W., Thomas, B. A. & Warner, E. M. (eds.) Astronomical Data Analysis Software and Systems XXVII*, vol. 523 of *Astronomical Society of the Pacific Conference Series*, 567 (2019).
56. Wright, J. T. & Eastman, J. D. Barycentric Corrections at  $1 \text{ cm s}^{-1}$  for Precise Doppler Velocities. *Publ. Astron. Soc. Pacif.* **126**, 838 (2014).
57. Rucinski, S. M. *et al.* Radial Velocity Studies of Close Binary Stars. VII. Methods and Uncertain-ties. *Publ. Astron. Soc. Pacif.* **124**, 1746–1756 (2002).

58. Tofflemire, B. M., Mathieu, R. D. & Johns-Krull, C. M. Accretion Kinematics in the T Tauri Binary TWA 3A: Evidence for Preferential Accretion onto the TWA 3A Primary.. *stron. J.* **158**, 245 (2019).
59. Tofflemire, B. M. offlemire/saphires: Zenodo archive (2019).
60. Husser, T.-O. *et al.* A new extensive library of PHOENIX stellar atmospheres and synthetic spectra. *Astron. Astrophys.* **553**, A6 (2013).
61. Spina, L. *et al.* The Gaia-ESO Survey: the present-day radial metallicity distribution of the Galactic disc probed by pre-main-sequence clusters. *Astron. Astrophys.* **601**, A70 (2017).
62. D’Orazi, V., Biazzo, K. & Randich, S. Chemical composition of the Taurus-Auriga association. *Astron. Astrophys.* **526**, A103 (2011).
63. Herczeg, G. J. & Hillenbrand, L. A. An Optical Spectroscopic Study of T Tauri Stars. I. Photospheric Properties.. *Astrophys. J.* **786**, 97 (2014).
64. Mann, A. W. *et al.* Zodiacial Exoplanets in Time (ZEIT). III. A Short-period Planet Orbiting a Pre-main-sequence Star in the Upper Scorpius OB Association. *Astron. J.* **152**, 61 (2016).
65. Mann, A. W. *et al.* TESS Hunt for Young and Maturing Exoplanets (THYME). VI. An 11 Myr Giant Planet Transiting a Very-low-mass Star in Lower Centaurus Crux. *Astron. J.* **163**, 156 (2022).
66. Rayner, J. T., Cushing, M. C. & Vacca, W. D. The Infrared Telescope Facility (IRTF) Spectral Library: Cool Stars. *Astrophys. J. Suppl.* **185**, 289–432 (2009).
67. Mann, A. W., *et al.* How to Constrain Your M Dwarf: Measuring Effective Temperature, Bolometric Luminosity, Mass, and Radius. *Astrophys. J.* **804**, 64 (2015).
68. Gaidos, E. *et al.* Trumpeting M dwarfs with CONCH-SHELL: a catalogue of nearby cool host-stars for habitable exoplanets and life. *Mon. Not. R. Astron. Soc.* **443**, 2561–2578 (2014).
69. Lantz, B. *et al.* SNIFS: a wideband integral field spectrograph with microlens arrays. In Mazuray, L., Rogers, P. J. & Wartmann, R. (eds.) *Optical Design and Engineering*, vol. 5249 of *Society of Photo-Optical Instrumentation Engineers (SPIE) Conference Series*, 146–155 (2004).
70. Allard, F. *et al.* Progress in modeling very low mass stars, brown dwarfs, and planetary mass objects. *Memorie della Societa Astronomica Italiana Supplementi* **24**, 128 (2013).
71. Gully-Santiago, M. A. *et al.* Placing the Spotted T Tauri Star LkCa 4 on an HR Diagram. *Astrophys. J.* **836**, 200 (2017).
72. Thao, P. C. *et al.* Hazy with a Chance of Star Spots: Constraining the Atmosphere of Young Planet K2-33b. *Astron. J.* **577**, A42 (2015).

73. Koen, C. The Seventeenth Data Release of the Sloan Digital Sky Surveys: Complete Release of MaNGA, MaStar, and APOGEE-2 Data. *Mon. Not. R. Astron. Soc.* **463**, 4383-4395 (2016).
74. Frasca, A. *et al.* REM near-IR and optical photometric monitoring of pre-main sequence stars in Orion. Rotation periods and starspot parameters. *Astron. Astrophys.* **508**, 1313-1330 (2009).
75. Thao, P.C. *et al.* Zodiacal Exoplanets in Time (ZEIT). IX. A Flat Transmission Spectrum and a Highly Eccentric Orbit for the Young Neptune K2-25b as Revealed by Spitzer. *Astron. J.* **159**, 2 (2020).
76. Baraffe, I., Homeier, D., Allard, F. & Chabrier, G. New evolutionary models for pre-main sequence and main sequence low-mass stars down to the hydrogen-burning limit. *Astron. Astrophys.* **577**, A42 (2015).
77. Foreman-Mackey, D., Hogg, D. W., Lang, D. & Goodman, J. The MCMC Hammer. *Publ. Astron. Soc. Pacif.* **125**, 306-312 (2013).
78. López-Valdivia, R. *et al.* The IGRINS YSO Survey. I. Stellar Parameters of Pre-main-sequence Stars in Taurus-Auriga. *Astrophys. J.* **921**, 53 (2021).
79. Hartmann, L., Herczeg, G. & Calvet, N. Accretion onto Pre-Main-Sequence Stars. *ARA&A* **54**, 135-180 (2016).
80. Alcalá, J. M. *et al.* X-shooter spectroscopy of young stellar objects in Lupus. Accretion properties of class II and transitional objects. *Astron. Astrophys.* **600**, A20 (2017).
81. Luhman, K. L. The Stellar Population of the Chamaeleon I Star-forming Region. *Astrophys. J. Suppl.* **173**, 104-136 (2007).
82. Kesseli, A. Y., Muirhead, P. S., Mann, A. W. & Mace, G. *et al.* Magnetic Inflation and Stellar Mass. II. On the Radii of Single, Rapidly Rotating, Fully Convective M-Dwarf Stars. *Astron. J.* **155**, 225 (2018).
83. Lavail, A., Kochukhov, O. & Hussain, G. A. J. Characterising the surface magnetic fields of T Tauri stars with high-resolution near-infrared spectroscopy. *Astron. Astrophys.* **630**, A99 (2019).
84. Masuda, K. & Winn, J. N. On the Inference of a Star's Inclination Angle from its Rotation Velocity and Projected Rotation Velocity. *Astron. J.* **159**, 81 (2020).
85. Tofflemire, B. M. *et al.* TESS Hunt for Young and Maturing Exoplanets (THYME). V. A Sub-Neptune Transiting a Young Star in a Newly Discovered 250 Myr Association. *Astron. J.* **161**, 171 (2021).

86. Raghavan, D. *et al.* A Survey of Stellar Families: Multiplicity of Solar-type Stars. *Astrophys. J. Suppl.* **190**, 1-42 (2010).
87. Lubow, S. H. & Ogilvie, G. I. On the Tilting of Protostellar Disks by Resonant Tidal Effects. *Astrophys. J.* **538**, 326–340 (2000).
88. Pearce, L. A. *et al.* Orbital Parameter Determination for Wide Stellar Binary Systems in the Age of Gaia. *Astrophys. J.* **894**, 115 (2020).
89. Blunt, S. *et al.* Orbits for the impatient: A bayesian rejection-sampling method for quickly fitting the orbits of long-period exoplanets. *Astron. J.* **153**, 229 (2017).
90. Ferrer-Chávez, R., Wang, J. J. & Blunt, S. Biases in Orbital Fitting of Directly Imaged Exoplanets with Small Orbital Coverage. *Astron. J.* **161**, 241 (2021).
91. Hildebrand, R. H. The determination of cloud masses and dust characteristics from submillimetre thermal emission. *QJRAS* **24**, 267–282 (1983).
92. Ansdell, M. *et al.* ALMA Survey of Lupus Protoplanetary Disks. I. Dust and Gas Masses. *Astrophys. J.* **828**, 46 (2016).
93. Beckwith, S. V. W., Sargent, A. I., Chini, R. S. & Guesten, R. A Survey for Circumstellar Disks around Young Stellar Objects. *Astron. J.* **99**, 924 (1990).
94. Testi, L. *et al.* The protoplanetary disk population in the  $\rho$ -Ophiuchi region L1688 and the time evolution of Class II YSOs. *Astron. Astrophys.* **663**, A98 (2022).
95. Mann, A. W. *et al.* Zodiacal Exoplanets in Time (ZEIT). I. A Neptune-sized Planet Orbiting an M4.5 Dwarf in the Hyades Star Cluster. *Astrophys. J.* **818**, 46 (2016).
96. Johnson, M. C. *et al.* K2-260 b: a hot Jupiter transiting an F star, and K2-261 b: a warm Saturn around a bright G star. *Mon. Not. R. Astron. Soc.* **481**, 596–612 (2018).
97. Kreidberg, L. BATMAN: BAsic Transit Model cAlculatioN in Python. *Publ. Astron. Soc. Pacif.* **127**, 1161–1165 (2015).
98. Foreman-Mackey, D., Agol, E., Ambikasaran, S. & Angus, R. *et al.* Fast and Scalable Gaussian Process Modeling with Applications to Astronomical Time Series.. *Astron. J.* **154**, 220 (2017).
99. Kipping, D. M. Efficient, uninformative sampling of limb darkening coefficients for two-parameter laws.. *Mon. Not. R. Astron. Soc.* **435**, 2152–2160 (2013).
100. Wittrock, J. M. *et al.* Transit Timing Variations for AU Microscopii b & c. *arXiv e-prints* arXiv:2202.05813 (2022).
101. Parviainen, H. & Aigrain, S.. LDTK: Limb Darkening Toolkit. *Mon. Not. R. Astron. Soc.* **453**, 3821–3826 (2015).

102. Van Eylen, V. & Albrecht, S. Eccentricity from Transit Photometry: Small Planets in Kepler Multi-planet Systems Have Low Eccentricities. *Astrophys. J.* **808**, 126 (2015).
103. Rogers, J. G., Janó Muñoz, C., Owen, J. E. & Makinen, T. L. Exoplanet atmosphere evolution: emulation with neural networks. *Mon. Not. R. Astron. Soc.* **519**, 6028–6043 (2023).
104. Marley, M. S. *et al.* The Sonora Brown Dwarf Atmosphere and Evolution Models. I. Model Description and Application to Cloudless Atmospheres in Rainout Chemical Equilibrium. *Astrophys. J.* **920**, 85 (2021).
105. Wood, M. L., Mann, A. W. & Kraus, A. L. Characterizing undetected stellar companions with combined datasets. *Astron. J.* **162**, 128 (2021).
106. Ansdel, M. *et al.* Young “Dipper” Stars in Upper Sco and Oph Observed by K2. *Astrophys. J.* **816**, 69 (2016).
107. Van Eyken, J. C. *et al.* The PTF Orion Project: A Possible Planet Transiting a T-Tauri Star.. *Astrophys. J.* **755**, 42 (2012).
108. Bouma, L. G. *et al.* PTFO 8-8695: Two Stars, Two Signals, No Planet. *arXiv e-prints* arXiv:2005.10253 (2020).
109. Stauffer, J. *et al.* Orbiting Clouds of Material at the Keplerian Co-rotation Radius of Rapidly Rotating Low-mass WTTs in Upper Sco. *Astron. J.* **153**, 152 (2017).
110. Koen, C. Multicolour time series photometry of the T Tauri star CVSO 30. *Mon. Not. R. Astron. Soc.* **450**, 3991–3998 (2015).
111. Ciardi, D. R. *et al.* Follow-up Observations of PTFO 8-8695: A 3 Myr Old T-Tauri Star Hosting a Jupiter-mass Planetary Candidate. *Astrophys. J.* **809**, 42 (2015).
112. Yu, L. *et al.* Tests of the Planetary Hypothesis for PTFO 8-8695b. *Astrophys. J.* **812**, 48 (2015).
113. Dattilo, A., Batalha, N. M. & Bryson, S. A A unified treatment of kepler occurrence to trace planet evolution. i. methodology. *Astron. J.* **166**, 122 (2023).
114. ExoFOP. Exoplanet follow-up observing program - kepler (2019).

**Acknowledgments** The authors thank Gregory Herczeg for providing the SNIFS spectrum of the host star. We also thank Sarah Blunt for her comments on the manuscript. Finally, we thank Halee and Bandit for their support during this project. M.G.B. was supported by NSF Graduate Research Fellowship (DGE-2040435), the NC Space Grant Graduate Research Fellowship, and the TESS Guest Investigator Cycle 5 program (21-TESS21-0016, PI D.D.). A.W.M. was supported by the NSF CAREER program (AST-2143763). M.D.F. is supported by an NSF Astronomy and Astrophysics Postdoctoral Fellowship (AST-2303911). D. D. acknowledges support from the TESS Guest Investigator Program (80NSSC23K0769).

M.F. was supported by NASA’s exoplanet research program (XRP 80NSSC21K0393). Funding for the TESS mission is provided by NASA’s Science Mission Directorate. We acknowledge the use of public TESS data from pipelines at the TESS Science Office and at the TESS Science Processing Operations Center. Resources supporting this work were provided by the NASA High-End Computing (HEC) Program through the NASA Advanced Supercomputing (NAS) Division at Ames Research Center for the production of the SPOC data products. TESS data presented in this paper were obtained from the Mikulski Archive for Space Telescopes (MAST) at the Space Telescope Science Institute. This work makes use of observations from the LCOGT network. This paper uses observations from the Habitable Zone Planet Finder on the Hobby Eberly Telescope at the McDonald Observatory.

**Author Contributions** M.G.B. identified the planet candidate, preformed the transit and false positive analysis, helped organize further analysis and observations, made most figures for the paper, and wrote large portions of the manuscript. A.W.M. estimated parameters of the host star and companion, organized LCO follow-up, helped with analysis of the ground-based photometry, and wrote large portions of the manuscript. A.V. wrote the light curve extraction pipeline to help identify the target and consulted on the pipeline’s outputs. D.K. analyzed the radial velocity from HPF and wrote the portion of the manuscript describing the analysis. A.K. helped organize the HPF observations, contributed to the LCO observation time, contributed NIRC2 observation time, analyzed the AO images, and contributed to the binary analysis. M.A. analyzed the disk and wrote the portion of the manuscript describing the analysis. L.P. analyzed the binary’s orbit and wrote the portion of the manuscript describing the analysis. G.M. fit the IGRINS data and extracted the radial velocities. G.M., D.J., and E.S. provided the IGRINS data. S.A. and C.E. provided the SMA data. A.B. calculated the rotation period and wrote the portion of the manuscript that describes the analysis. K.C., R.P.S., F.M., E.P. and C.N.W. contributed LCO observation time and reduced the data. M.D.F. aided in the Keck/NIRC2 observations. D.D. provided funding for the project during the planet discovery and characterization. A.F. created the schematic representation of the system. M.F. analyzed the  $V \sin(i_*)$ . A.I.L.M. analyzed the TTVs. E.R.N. aided in organizing follow-up observations. B.M.T. contributed to the LCO observation time, contributed NIRC2 observation time. P.C.T. contributed code to make the planet demographics plots. J.J. leads the SPOC which provided the calibrated FFI data and PDC and SAP light curves used in the analysis. J.J., D.L., G.R., S.S., R.V., and J.N.W. are TESS mission architects. D.C., Z.E., D.R.R., A.S., J.D.T., and J.N.V. are TESS mission contributors.

**Competing Interests** The authors declare that they have no competing financial interests.

**Correspondence** Correspondence and requests for materials should be addressed to Madyson Barber: madysonb@live.unc.edu.

Reprints and permissions information is available at [www.nature.com/reprints](http://www.nature.com/reprints).

Description	Parameter	Value		
		SDSS <i>g</i>	SDSS <i>i</i>	PS <i>z<sub>s</sub></i>
Planet-to-star radius ratio	$R_p/R_*$	$0.0647^{+0.0088}_{-0.009}$	$0.0696^{+0.006}_{-0.0063}$	$0.0703 \pm 0.0019$
Transit timing variation	$T_{0,O} - T_{0,C}$	$0.002 \pm 0.005$	$0.004 \pm 0.003$	$0.0 \pm 0.002$
Constant coefficient	<b>a</b>	$-0.0014 \pm 0.0011$	$-0.0027 \pm 0.0007$	$-0.0019 \pm 0.0004$
Linear coefficient	<b>b</b>	$0.0018^{+0.0116}_{-0.0110}$	$0.033^{+0.0062}_{-0.0061}$	$0.0085 \pm 0.0017$

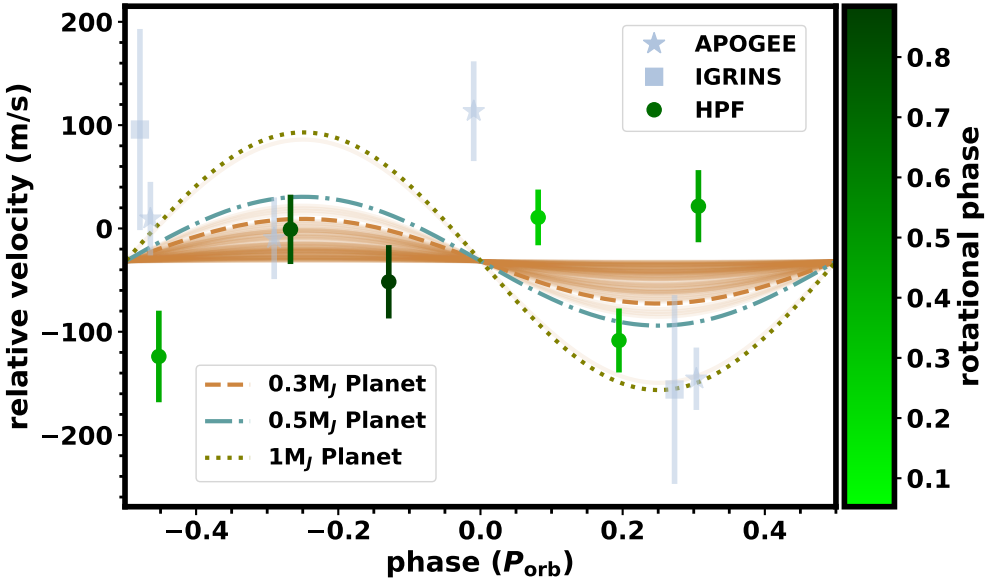
Extended Data Table 1: Ground-based transit and variability fit parameters.

Fit parameters of the simultaneous transit and variability models of the ground-based transits.

Epoch [BJD]	Separation [mas]	Position Angle [deg]
2455157.03	$4012.94 \pm 1.45$	$198.148 \pm 0.020$
2456881.12	$4009.26 \pm 1.44$	$198.158 \pm 0.021$
2460283.78	$3998.46 \pm 1.51$	$198.148 \pm 0.022$
2460283.78	$3997.12 \pm 1.42$	$198.148 \pm 0.020$

Extended Data Table 2: Keck/NIRC2 Astrometry

Astrometry values for TIC 56658273 measured with Keck/NICR2. A  $-0.062$  deg offset has been applied to position angle to convert from Keck/NIRC2 frame into Gaia DR3 frame.



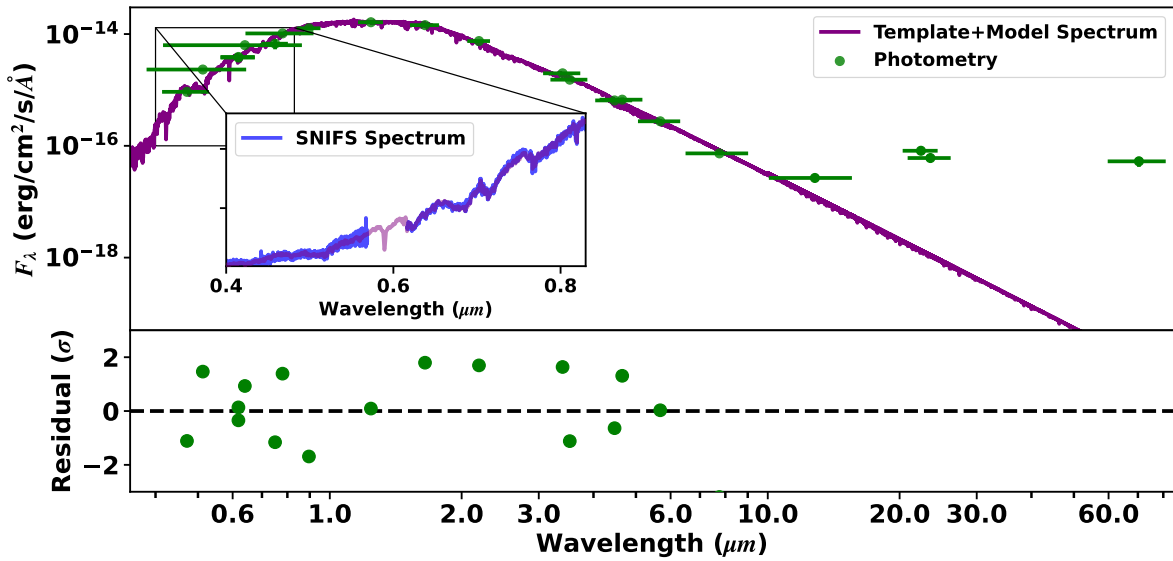
Extended Data Figure 1: Radial velocities and signal fit models

Radial velocities of IRAS 04125+2902 phased to the period of the planet. RVs from APOGEE are shown as stars, those from IGRINS are shown as squares, and those from HPF are shown as circles colored by the stellar rotation phase (with an arbitrary zero point). Error bars represent the  $1\sigma$  uncertainties. We show the expected signals from a 0.5 and 1  $M_J$  companion, as well as the 95% upper-mass limit ( $0.3 M_J$ ) and 100 random draws from the fit posterior. The long term RVs rule out any companion of stellar mass, and the best-fit of the HPF measurements constrains the planet's upper mass limit.

Epoch (BJD)	Absolute RV (km s <sup>-1</sup> )	$\sigma_{\text{Abs. RV}}$ (km s <sup>-1</sup> )	Relative RV (m s <sup>-1</sup> )	$\sigma_{\text{Rel. RV}}$ (m s <sup>-1</sup> )	Source
2457050.603	17.174	0.097	95.7	97.3	IGRINS
2458090.937	16.923	0.091	-155.9	91.4	IGRINS
2458499.666	17.088	0.036	9.5	35.6	APOGEE
2458503.684	17.192	0.048	113.5	48.3	APOGEE
2458744.995	16.933	0.030	-145.5	30.2	APOGEE
2458854.603	17.069	0.040	-9.5	39.5	APOGEE
2460306.817	16.91	0.10	10.7	27.0	HPF
2460307.821	16.87	0.11	-108.4	31.0	HPF
2460308.808	17.00	0.12	21.6	34.9	HPF
2460312.574	16.93	0.11	-0.9	33.6	HPF
2460313.795	16.98	0.13	-51.6	35.5	HPF
2460319.773	16.80	0.16	-123.9	44.3	HPF

Extended Data Table 3: Radial velocity measurements of IRAS 04125+2902

For IGRINS and APOGEE, the relative RVs are normalized to each other. For HPF, the relative RVs are the extracted values using the empirical template, as described in text. Times in Barycentric Dynamical Time, although epochs are not measured with sufficient precision to distinguish.



Extended Data Figure 2: SED fit of IRAS 04125+2902

Example fit to the SED and residuals (in  $\sigma$ ), showing a combination of a template and atmospheric model (purple) compared to the observed photometry (green). The vertical errors are the photometric uncertainties (in almost all cases, smaller than the size of the symbol), while the horizontal error bars indicate the width of the filter. The inset shows the template compared to the observed SNIFS spectrum of IRAS 04125+2902.

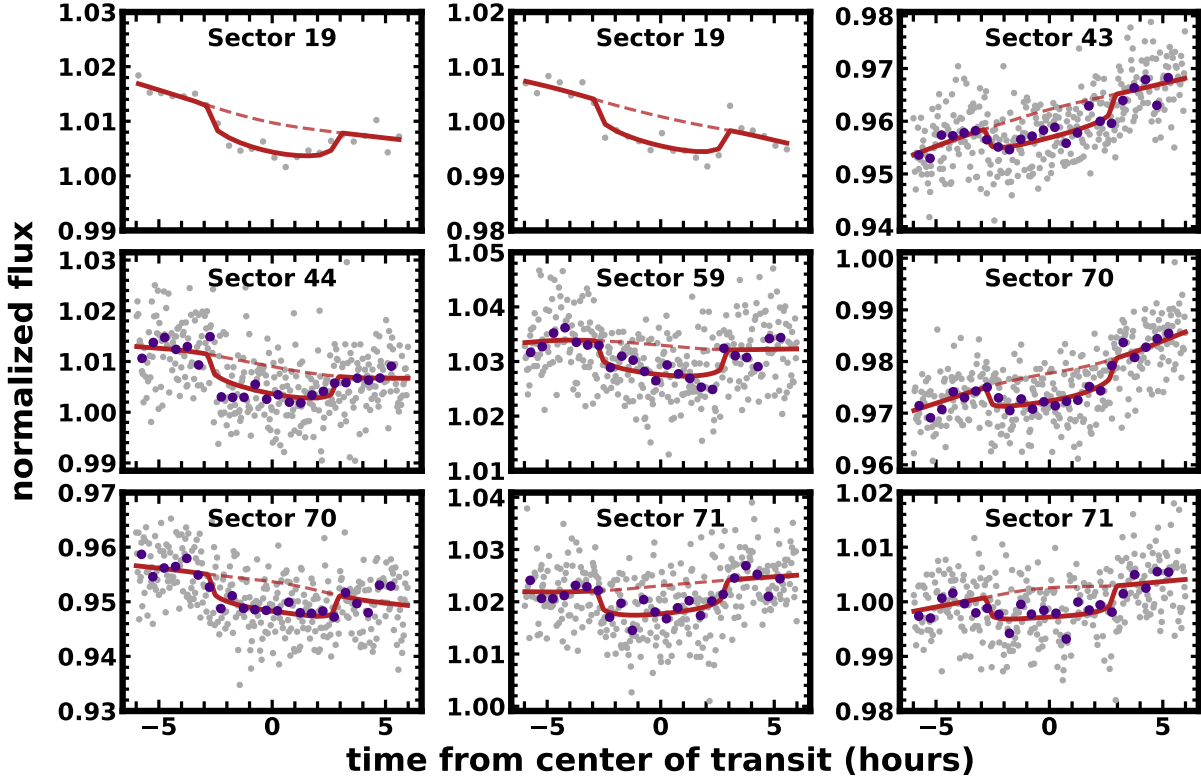
Description	Parameter	Value
Measured Parameters		
Initial transit mid-point	$T_0$ (BJD-TBD)	$2458821.8251 \pm 0.0033$
Orbital Period	$P$ (days)	$8.834978 \pm 2.8 \times 10^{-5}$
Planet-to-star radius ratio	$R_P/R_\star$	$0.0679^{+0.0028}_{-0.0025}$
Impact parameter	$b$	$0.34^{+0.24}_{-0.23}$
Stellar density	$\rho_\star (\rho_\odot)$	$0.256^{+0.047}_{-0.087}$
<i>TESS</i> limb-darkening coefficient	$q_{1,1}$	$0.29^{+0.17}_{-0.14}$
<i>TESS</i> limb-darkening coefficient	$q_{2,1}$	$0.321^{+0.098}_{-0.1}$
GP Parameters		
Natural logarithm of period	$\ln(P)$	$2.52^{+0.16}_{-0.15}$
Natural logarithm of amplitude	$\ln(\text{amp})$	$-5.82^{+0.18}_{-0.2}$
Quality factor	$\ln(Q)$	$0.564^{+0.031}_{-0.021}$
Derived Parameters		
Semi-major axis to stellar radius ratio	$a/R_\star$	$11.42^{+0.66}_{-1.0}$
Orbital inclination	$i$ ( $^\circ$ )	$88.3^{+1.2}_{-1.6}$
Transit duration (first to fourth contact)	$T_{14}$ (days)	$0.2498^{+0.007}_{-0.0054}$
Planet radius	$R_P (R_J)$	$0.958^{+0.077}_{-0.075}$
Semi-major axis	$a$ (AU)	$0.077^{+0.0069}_{-0.01}$
Equilibrium temperature <sup>†</sup>	$T_{\text{eq}}$ (K)	$854.0^{+59.0}_{-32.0}$

† assuming zero albedo

Extended Data Table 4: Properties of IRAS 04125+2902 b  
 Planet and orbital parameters derived from the *TESS* light curve transit analysis

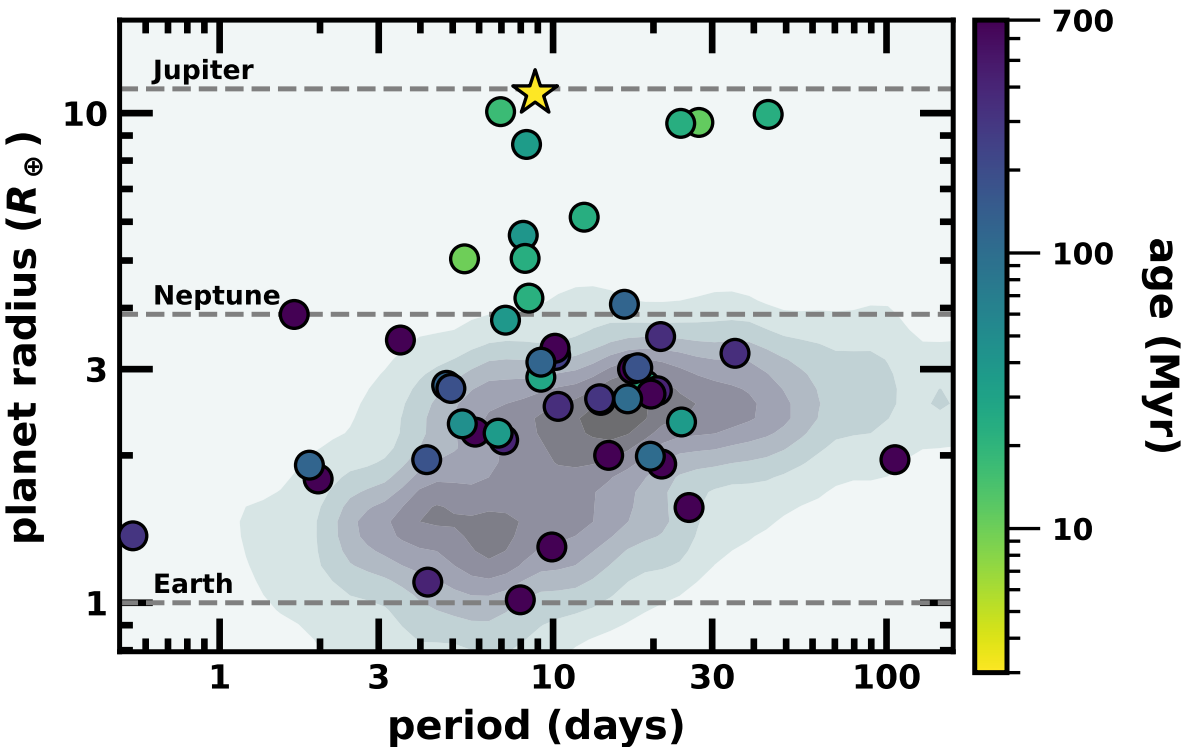
Parameter	Host	Companion	Source
Identifiers			
IRAS	04125+2902	...	IRAS
Gaia	164800235906366976	164800235906367232	Gaia DR3
TIC	56658270	56658273	TESS
TOI	6963	...	TESS
2MASS	J04154278+2909597	J04154269+2909558	2MASS
ALLWISE	J041542.77+290959.5	...	ALLWISE
Astrometry			
$\alpha$	63.928341	63.927944	Gaia DR3
$\delta$	29.166539	29.165482	Gaia DR3
$\mu_\alpha$ (mas yr $^{-1}$ )	$12.104 \pm 0.035$	$12.56 \pm 0.16$	Gaia DR3
$\mu_\delta$ (mas yr $^{-1}$ )	$-18.145 \pm 0.023$	$-17.19 \pm 0.11$	Gaia DR3
$\pi$ (mas)	$6.247 \pm 0.027$	$6.26 \pm 0.12$	Gaia DR3
Photometry			
TESS (mag)	$12.8131 \pm 0.0068$	$15.619 \pm 0.013$	TESS
$G_{Gaia}$ (mag)	$13.9814 \pm 0.0017$	$17.4450 \pm 0.0015$	Gaia DR3
$BP_{Gaia}$ (mag)	$15.595 \pm 0.007$	$20.64 \pm 0.13$	Gaia DR3
$RP_{Gaia}$ (mag)	$12.738 \pm 0.004$	$15.832 \pm 0.007$	Gaia DR3
$u'$ (mag)	$19.718 \pm 0.003$	$23.371 \pm 0.441$	SDSS DR16
$g'$ (mag)	$16.811 \pm 0.004$	$22.986 \pm 0.154$	SDSS DR16
$r'$ (mag)	$14.652 \pm 0.003$	$20.128 \pm 0.028$	SDSS DR16
$i'$ (mag)	$13.648 \pm 0.001$	$16.805 \pm 0.005$	SDSS DR16
$z'$ (mag)	$12.568 \pm 0.003$	$15.259 \pm 0.005$	SDSS DR16
$J$ (mag)	$10.709 \pm 0.029$	$12.726 \pm 0.034$	2MASS
$H$ (mag)	$9.756 \pm 0.030$	$11.807 \pm 0.041$	2MASS
$K_s$ (mag)	$9.376 \pm 0.028$	$11.288 \pm 0.028$	2MASS
$W1$ (mag)	$9.192 \pm 0.030$	...	ALLWISE
$W2$ (mag)	$9.096 \pm 0.032$	...	ALLWISE
$W3$ (mag)	$8.714 \pm 0.037$	...	ALLWISE
$W3$ (mag)	$4.739 \pm 0.026$	...	ALLWISE
Physical Properties			
$P_{rot}$ (days)	$11.31 \pm 0.06$	...	This work
$v \sin i_*$ (km s $^{-1}$ )	$7.1 \pm 0.5$	...	This work
$i_*$ ( $^\circ$ )	> 78	...	This work
$F_{bol}$ (erg cm $^{-2}$ s $^{-1}$ )	$(5.8 \pm 0.5) \times 10^{-10}$	$(6.6 \pm 0.5) \times 10^{-11}$	This work
$T_{eff}$ (K)	$4080 \pm 95$	$2830 \pm 90$	This work
$A_V$ (mag)	$2.71 \pm 0.20$	$2.85 \pm 0.25$	This work
$R_*$ ( $R_\odot$ )	$1.45 \pm 0.10$	$0.96 \pm 0.12$	This work
$L_*$ ( $L_\odot$ )	$0.466 \pm 0.041$	$0.050 \pm 0.004$	This work
$M_*$ ( $M_\odot$ )	$0.70 \pm 0.04$	$0.17 \pm 0.04$	This work
Age (Myr)	$3.3^{+0.6}_{-0.5}$		This work

Extended Data Table 5: Parameters of the host star and companion  
Properties of the host star IRAS 04125+2902 and wide binary companion TIC 56658273



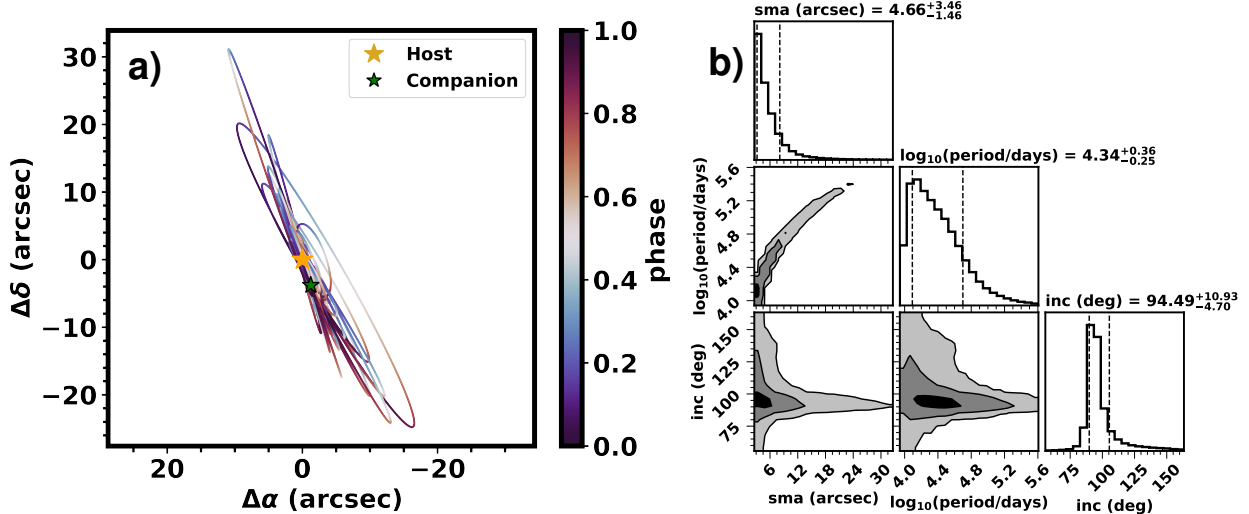
Extended Data Figure 3: Individual transits of IRAS 04125+2902 b from *TESS*

Representative transits from each *TESS* sector (gray points). SPOC data in sectors 43, 44, 59, 70, and 71 are binned to 30 minute intervals (purple points) for a fair comparison to sector 19 (30-minute FFI only). The combined GP and transit model is shown as the solid red line with a dashed line showing the GP fit without the transit.



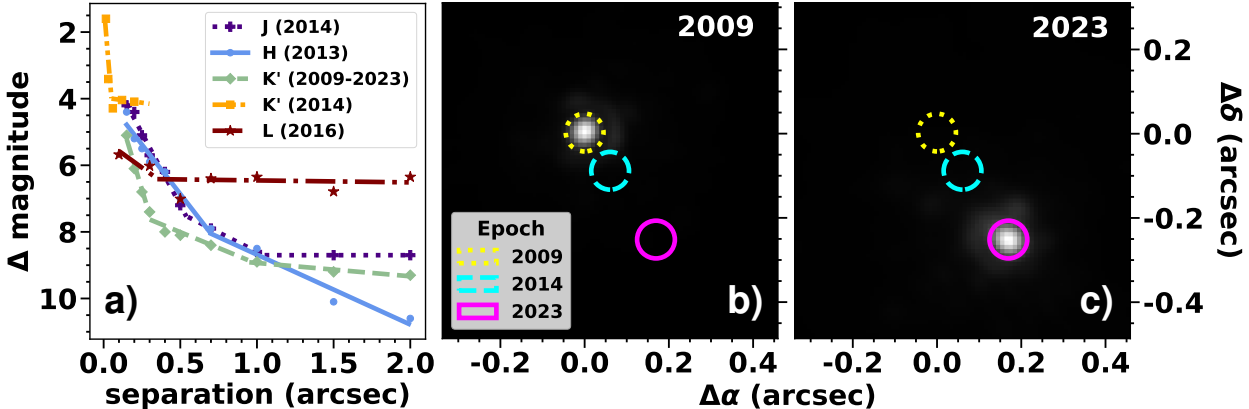
Extended Data Figure 4: IRAS 04125+2902 b in comparison to other transiting systems

The contour distribution of (primarily older) planets discovered by Kepler and *K2*<sup>113</sup> overlapped with the young ( $< 700$  Myr) transiting systems discovered in a cluster or association. The young planets are colored by their approximate age in log space. IRAS 04125+2902 b is marked with a star and sits high in radius compared to older systems. Planet properties from<sup>114</sup>.



Extended Data Figure 5: Orbital properties of the binary companion

**a)** 100 random fits of the orbit of TIC 56658273 colored by the orbital phase. The orange star represents the location of the host star, IRAS 04125+2902, and the green stars represent the measured relative locations of TIC 56658273. The  $1\sigma$  uncertainties of the locations of TIC 56658273 are smaller than the data points, and the individual locations are indistinguishable at this scale. **b)** Corner plot of the parameters of the wide binary companion. The dashed lines represent the 16th and 84th percentile of the distribution. 99% of points are shown for clarity. The inclination of the orbit is highly consistent with edge-on.



Extended Data Figure 6: Imaging data of IRAS 04125+2902

**a)** Contrasts from high-resolution data. We show the deepest data for each band, but additionally separating  $K$ -band imaging (green) and  $K$ -band NRM (yellow) as they cover different angular separations. A simple break-point linear fit for each band is shown for clarity. **b & c)** AO images from Keck/NIRC2 of IRAS 04125+2902 across 2 epochs with circles representing the previous/future locations: 2009 (dotted yellow), 2014 (dashed blue), and 2023 (solid pink). Based on the *Gaia* proper motions, the star has moved  $\sim 305$  mas ( $6 \lambda/D$ ) over the 14 year period spanned by the Keck/NIRC2 data, which is greater than the PSF width of the star. We can see there are no stars coming in or out of view that could be causing the observed transit signal.